Effects of Concurrent Irradiation with Ions and Electrons on Cascade Damages in Non-metallic Inorganic Crystals

阿部, 弘亨
Graduate School of Engineering, Kyushu University

https://doi.org/10.11501/3065528

出版情報：九州大学, 1992, 博士（工学）, 課程博士
バージョン：
権利関係：

5.4. EFFECTS OF CONCURRENT IRRADIATION WITH IONS AND ELECTRONS ON ACCUMULATION OF CASCADE DAMAGES

Fast neutrons simultaneously induce cascade damages, isolated point defects, athermal migration of point defects and electronic excitation, and they may introduce concurrent effects on the radiation damage process. The HVEM-ACC facility is one of suitable facilities to get insights into the concurrent effect of ions and electrons on the radiation damage process. The HVEM-ACC facility, therefore, was extensively used for getting information about the concurrent irradiation effects of electrons on the accumulation process of cascade damages in Ge and Si.

Figure 5.4 shows sequential micrographs showing accumulation of cascade contrasts in Ge irradiated with 30keV Xe^+ ions. Cascade damages show up their contrasts and increase in their number as increasing the irradiation time. The electron dose rate does not change cascade contrasts themselves at the early stage of irradiation. However, some of cascade contrasts annihilate under continuous ion and electron irradiation for a few tens of seconds as indicated with arrows in the figure. The annihilation can be observed through shrinkage of cascade contrasts. The cascade contrasts are obviously caused by ion irradiation, while the annihilation of cascade contrasts is presumably done by electron irradiation. The life time of those cascade contrasts is about a few tens of seconds which is very much longer than that for Cu [11] and Au [27]. The life time of the cascade contrasts under dual-beam irradiation is related to the absorption rate of point defects and the

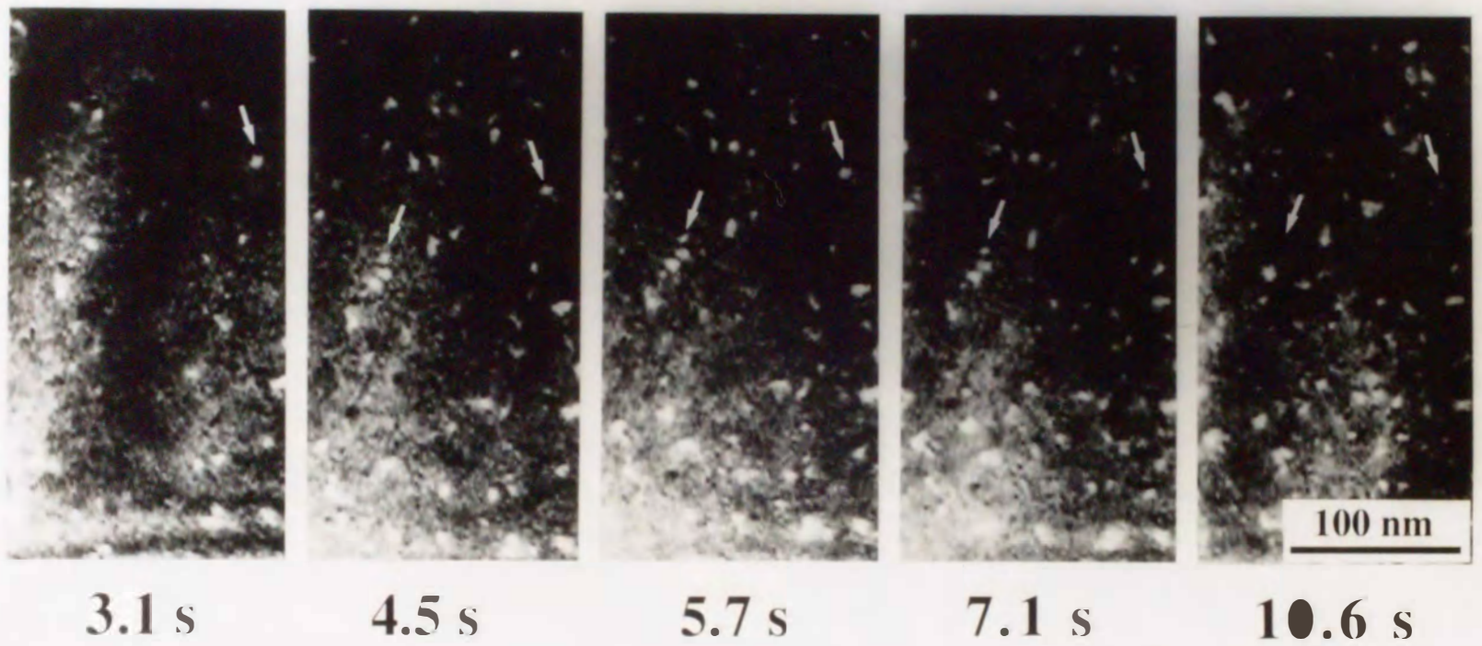

Figure 5.4 A sequence of weak-beam dark-field images on TV monitor showing evolution of cascade contrasts in Ge irradiated with a 30keV Xe^+ ion dose rate of 5.0×10^{15} ions/m^2s and a 1MeV electron dose rate of 1.8×10^{23} e/m^2s. Some of cascade contrasts as indicated by arrows disappeared during irradiation.

athermal migration of point defects introduced by electrons, which will be discussed in detail in **chapter 7.**

The area density of the cascade contrasts was measured to clarify the concurrent irradiation effects of ions and electrons on the accumulation process of cascade damages. **Figure 5.5** shows typical accumulation curves of the area density of cascade damages in (a) Si irradiated with 60keV Ar^{2+} ions, (b) Ge irradiated with 30keV Xe^{+} ions and (c) and (d) Ge irradiated with 30keV Ar^{+} ions. In those experiments the statistical error of the area density was from 30 to 10% with increasing the area density from 10^{14} to 10^{16} m^{-2}, while the error of irradiation time was less than 0.5s. The cascade contrasts increase in their number within a few seconds following $(\phi t)^{x}$ at the early stage of irradiation. The values of x depend on the combination of the projectiles and targets; namely x=1.4 for (a), x=1.5 for (b), x=1.2 for (c) and x=1.7 for (d). One can see the obvious difference between (c) and (d) even though both of their combination of projectiles and target atoms and the nominal ion dose rate are the same. A possible reason is thought to be very low actual ion dose rate in (c) in contrast to (d), since the accumulation process is sensitive to the ion dose rate especially at the early stage of irradiation. The dose rate effect on the initial accumulation process will be described later in detail.

The power x scarcely depends on electron dose rate. In contrast to the early stage of the accumulation process, clearly shown in **figure 5.5** is a decrease in the saturation density with increasing electron dose rate. This is a kind of concurrent effects of electron irradiation on the accumulation process of cascade damages. The saturation density is consistent with the in-situ

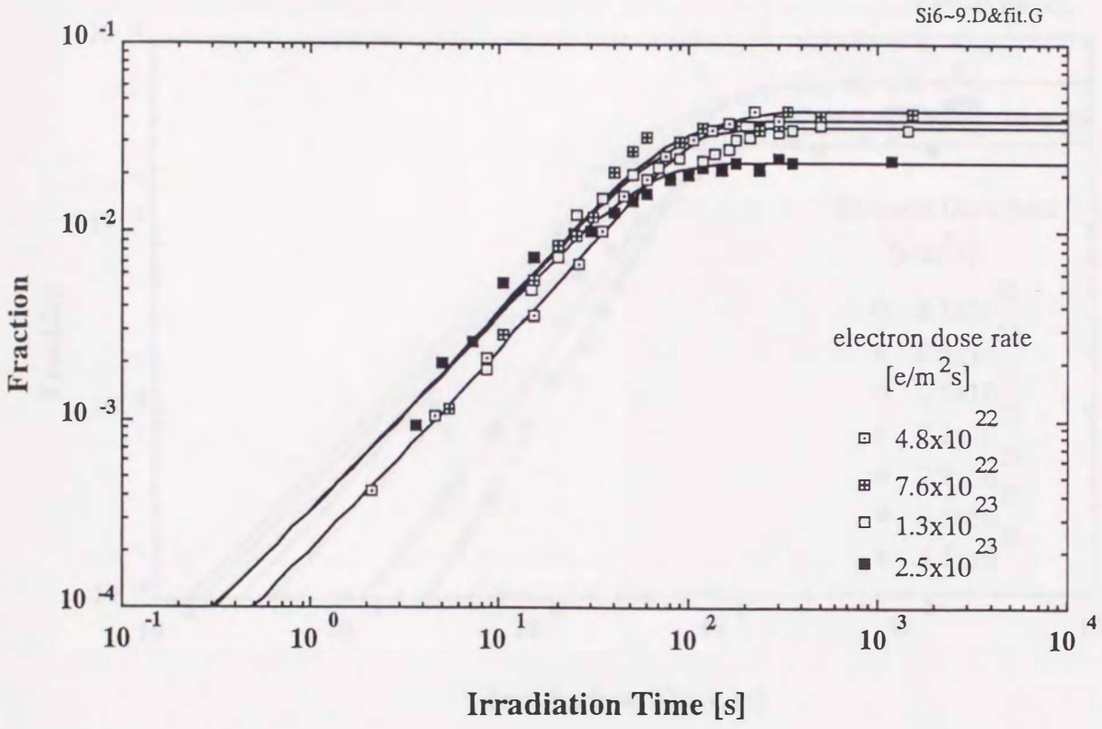

Figure 5.5 (a) The density of cascade contrasts as a function of ion dose in Si irradiated with 60keV Ar^{2+} ions and 1MeV electrons.

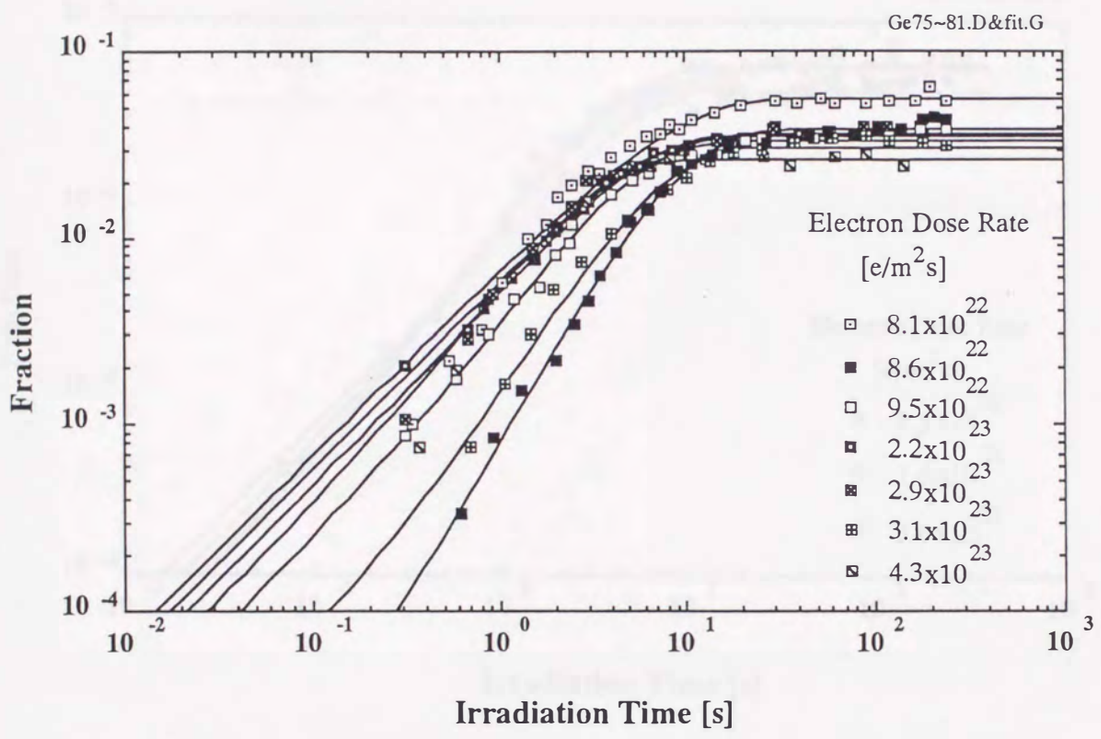

Figure 5.5 (b) Same as in (a), but for Ge irradiated with 30keV Xe^+ ions and 1MeV electrons.

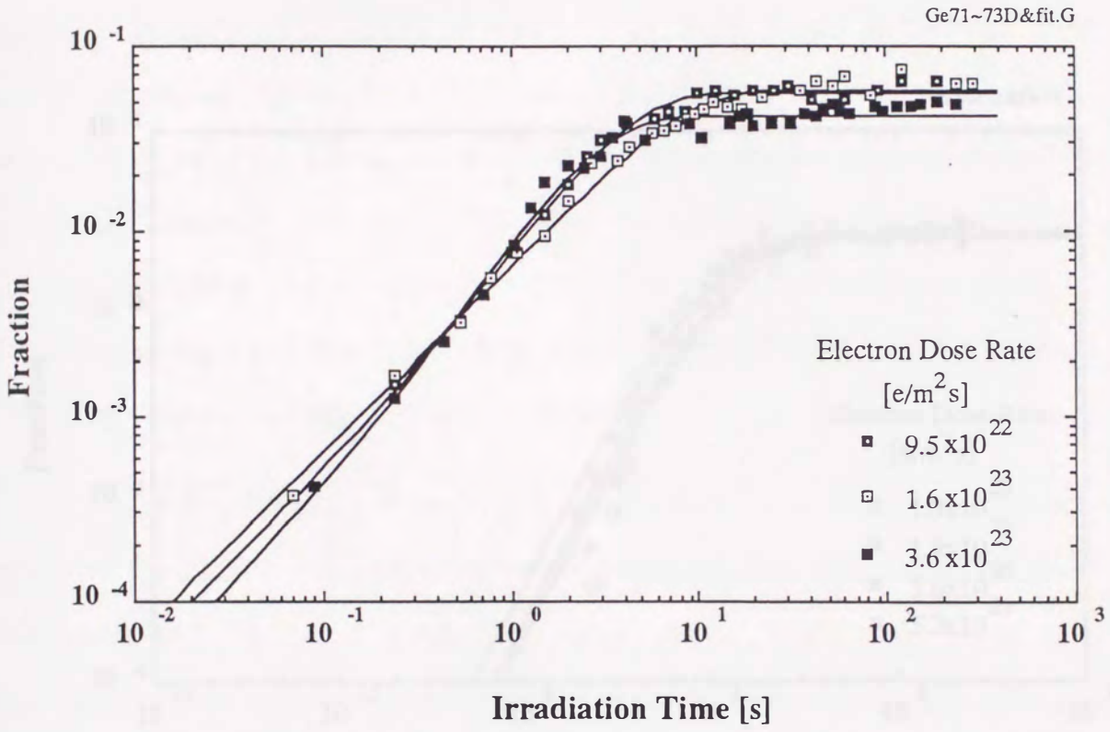

Figure 5.5 (c) Same as in (a), but for Ge irradiated with 30keV Ar^+ ions and 1MeV electrons.

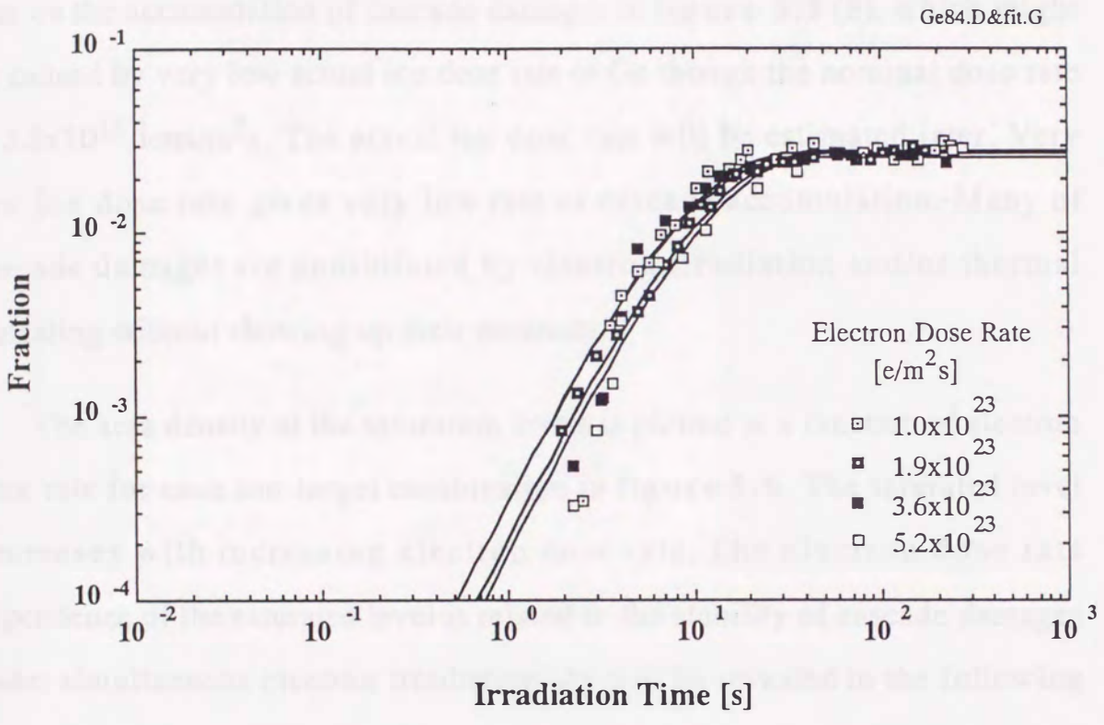

Figure 5.5 (d) Same as in (a), but for Ge irradiated with 30keV Ar^+ ions and 1MeV electrons.

observation which indicates the annihilation of cascade contrasts during dual-beam irradiation. The annihilation of cascade contrasts is presumably caused by electron irradiation. As emphasized in **chapter 2** and will be discussed in **chapter 6**, the cascade annihilation would be caused not only by the absorption of interstitial atoms but also by the electron-induced migration of vacancies and interstitial atoms. One can see no dependence of electron dose rate on the accumulation of cascade damages in **figure 5.5** (d), which might be caused by very low actual ion dose rate in Ge though the nominal dose rate is 2.3×10^{15} ions/m^2s. The actual ion dose rate will be estimated later. Very low ion dose rate gives very low rate of cascade accumulation. Many of cascade damages are annihilated by electron irradiation and/or thermal annealing without showing up their contrasts.

The area density at the saturation levels is plotted as a function of electron dose rate for each ion-target combination in **figure 5.6**. The saturated level decreases with increasing electron dose rate. The electron dose rate dependence of the saturated level is related to the stability of cascade damages under simultaneous electron irradiation. As will be revealed in the following paragraphs, the saturated levels depend not only electron dose rate but also actual ion dose rate.

Based on the model (2) in the previous section and on the previous discussion, we can construct kinetic equations which describe the effect of simultaneous electron irradiation on the accumulation process of cascade damages. Electrons induce the retardation of accumulation of cascade damages. The annihilation of amorphous and predamaged regions contributes to increase undamaged regions whose concept is supported by Nastasi and

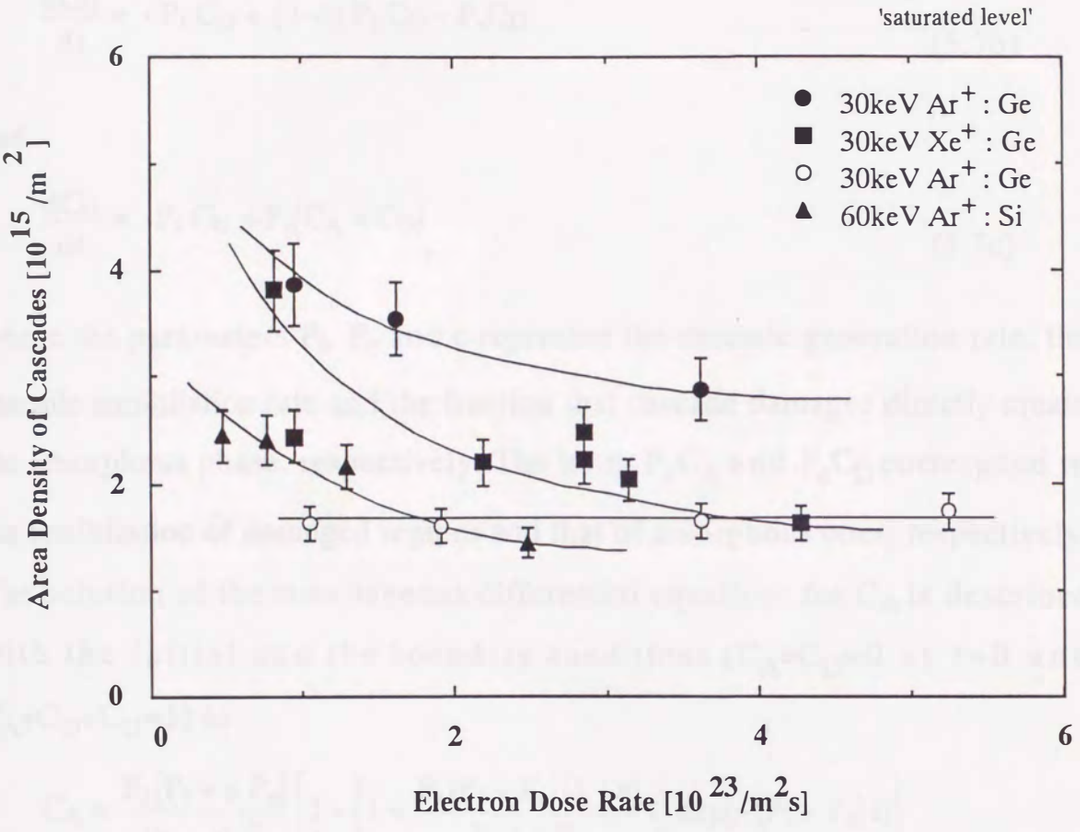

Figure 5.6 The saturated area density of cascades in Si and Ge as a function of 1MeV electron dose rate for various irradiation conditions.

Mayer [131]. The annihilation terms of amorphous and predamaged regions are, therefore, added to eq. (5.3). The basic equations are

$$\frac{dC_A}{dt} = P_i C_D + cP_i C_U - P_e C_A \qquad (5.7a)$$

$$\frac{dC_D}{dt} = - P_i C_D + (1-c) P_i C_U - P_e C_D \qquad (5.7b)$$

and

$$\frac{dC_U}{dt} = -P_i C_U + P_e(C_A + C_D), \qquad (5.7c)$$

where the parameters P_i, P_e and c represent the cascade generation rate, the cascade annihilation rate and the fraction that cascade damages directly create the amorphous phase, respectively. The terms $P_e C_A$ and $P_e C_D$ correspond to the annihilation of damaged regions and that of amorphous ones, respectively. The solution of the simultaneous differential equations for C_A is described with the initial and the boundary conditions ($C_A=C_D=0$ at $t=0$ and $C_A+C_D+C_U=1$) as

$$C_A = \frac{P_i(P_i + c P_e)}{(P_i + P_e)^2}\left[1 - \left\{1 + \frac{P_i(P_i + P_e)(1 - c)}{P_i + c P_e} t\right\} \exp\{-(P_i + P_e) t\}\right]. \qquad (5.8)$$

The saturation level of the eq. (5.8) C_A^0 is expressed as functions of P_i, P_e and c by

$$C_A^0 = \frac{P_i(P_i + c P_e)}{(P_i + P_e)^2}. \qquad (5.9)$$

The time variation of C_A was calculated from the eq. (5.8) with use of the parameters P_i, P_e and c. **Figure 5.7** (a), (b) and (c) show the result on C_A as functions of parameters (a) P_i, (b) P_e and (c) c, respectively. Each result

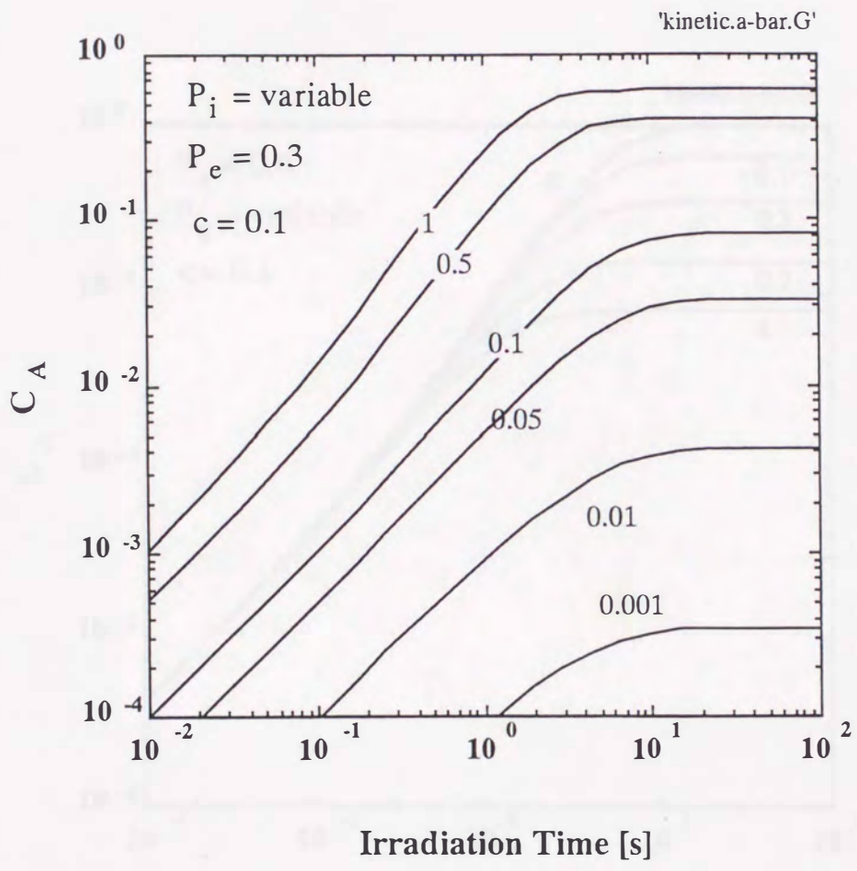

Figure 5.7 (a) Values of the fraction of amorphous, C_A, plotted against irradiation time for various combinations of parameters for P_i being variables.

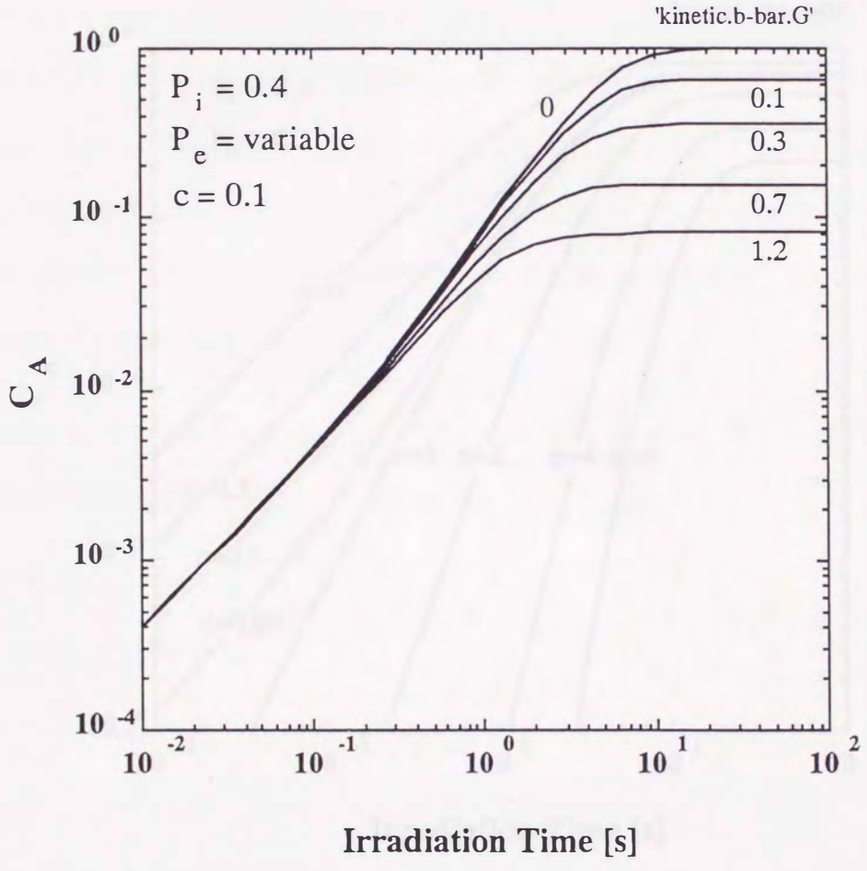

Figure 5.7 (b) Values of the fraction of amorphous, C_A, plotted against irradiation time for various combinations of parameters for P_e being variables.

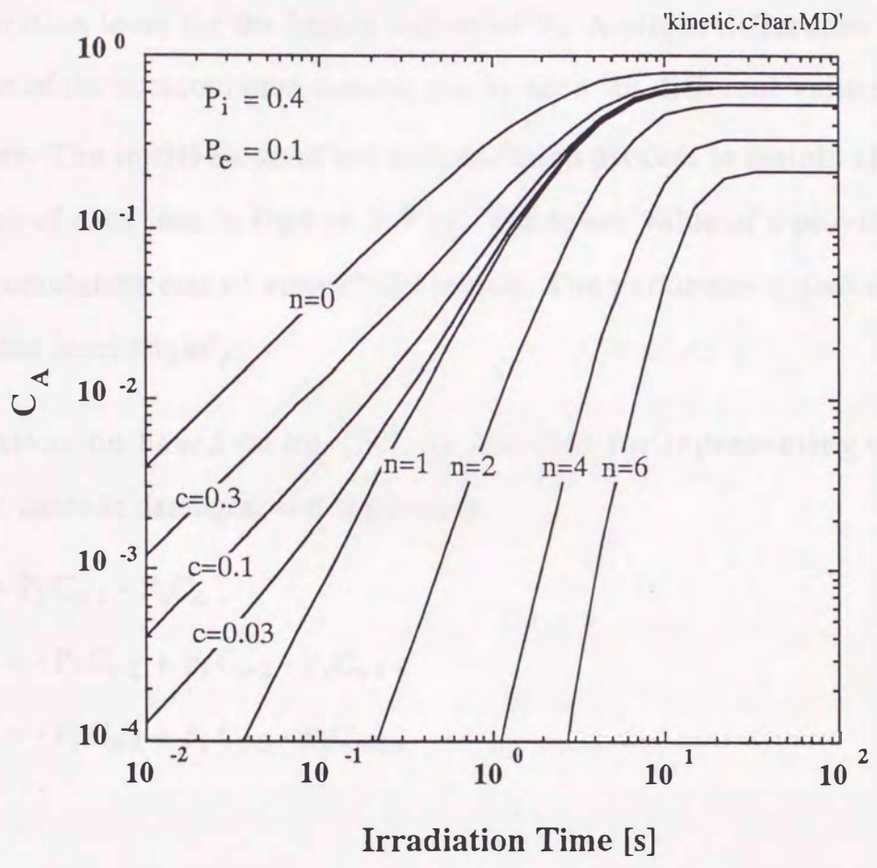

Figure 5.7 (c) Values of the fraction of amorphous, C_A, plotted against irradiation time for various combinations of parameters for c and n being variables.

shows the accumulation of amorphous fraction eventually leading to saturation. The parameter P_i affects the accumulation rate of amorphous and the saturation level. With increasing the value of P_i, the accumulation rate and the saturation level become higher. As for the parameter P_e, its effect is mainly on the saturation level. Obviously shown in **figure 5.7** (b) is the lower saturation level for the higher values of P_e. A slight difference in the initial slope of the accumulation process can be seen for different values of P_e in the figure. The initial slope of the accumulation process is mainly affected by the value of c, as seen in **figure 5.7** (c). The lower value of c provides the higher accumulation rate of amorphous region. The parameter c also affects the saturation level slightly.

An extension based on eq. (5.5) is possible for representing n-tuple overlaps of cascade damages, and is given as

$$\frac{dC_A}{dt} = P_i C_{n-1} - P_e C_A ,$$
$$\frac{dC_{n-1}}{dt} = - P_i C_{n-1} + P_i C_{n-2} - P_e C_{n-1} ,$$
$$\frac{dC_{n-2}}{dt} = - P_i C_{n-2} + P_i C_{n-3} - P_e C_{n-2} ,$$
$$\cdots\cdots$$
$$\cdots\cdots$$
$$\frac{dC_2}{dt} = - P_i C_2 + P_i C_1 - P_e C_2 ,$$
$$\frac{dC_1}{dt} = - P_i C_1 + P_i C_U - P_e C_1$$

and

$$\frac{dC_U}{dt} = - P_i C_U + P_e C_A + \sum_{i=1}^{n-1} P_e C_i \quad . \qquad (5.10)$$

The Laplace transformation of eq. (5.10) in terms of a matrix gives the solution of C_A as

$$C_A = \left(\frac{P_i}{P_i + P_e}\right)^{n+1} \left[1 - \sum_{k=0}^{n} \frac{\{(P_i+P_e)\,t\}^k}{k!} \exp\{-(P_i + P_e)\,t\} \right]. \qquad (5.11)$$

The time variation of C_A was calculated from this equation in terms of the parameter n, and it is shown in **figure 5.7 (c)**.

Eqs. (5.8) and (5.11) describe the accumulation process of amorphous phase and the annihilation process of amorphous and damaged phases. The solid lines in **figure 5.5** are theoretical values calculated from eqs (5.8) and (5.11) so as to provide the best fit to the experimental results. In order to compare C_A with the area density of cascades, the density is converted into non-dimensional fraction with use of the measured diameter of cascade contrasts.

Figure 5.8 shows one of other examples of the parametric fitting curves. Open circles are corresponding to experimental data on the accumulation of cascade contrasts. The best fitted curve with parameters (P_i, P_e, c) = (0.06, 0.3, 0.04) is shown as the solid curve together with other ones, which are close to the best fitted curve. The least square method [132] was employed for fitting eq. (5.8) and (5.11) to the experimental data. Some of the experimental data were fitted with eye taking into account the slope and the saturation level. The parameter P_i is the intrinsic formation rate of cascade damages which is corresponding to the actual ion dose rate under irradiation with relatively low energy ions. Therefore, the difference between the values

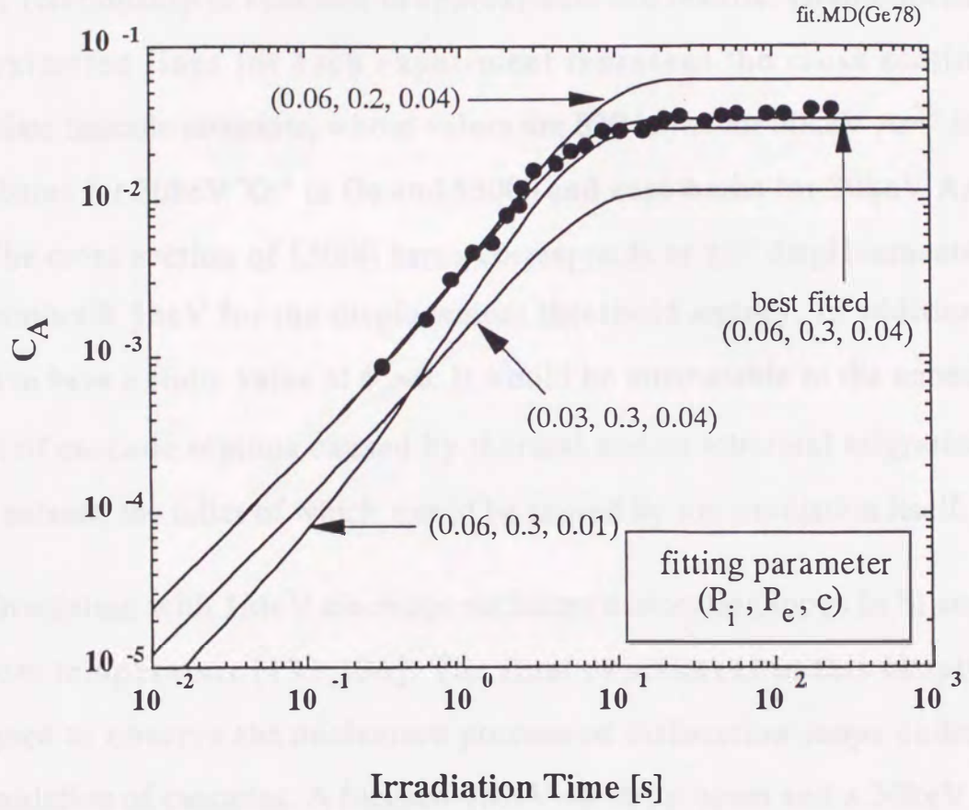

Figure 5.8 An example of fitting for Ge irradiated with 30keV Xe^+ ion dose rate of 3.0×10^{15} ions/m^2s and 1MeV electron dose rate of 2.2×10^{23} e/m^2s.

of P_i in figure 5.5 (c) and (d) comes from the intrinsic difference between ion dose rates, though nominal ion dose rates are the same.

The electron dose rate dependence of the parameter P_e is shown in **figure 5.9**. The value of P_e increases with increasing electron dose rate. Linear relationship is assumed to approximate the results. Gradients of the approximated lines for each experiment represent the cross section to annihilate cascade contrasts, whose values are 830 barns for 60keV Ar^{2+} in Si, 8800 barns for 30keV Xe^+ in Ge and 13000 and zero barns for 30keV Ar^+ in Ge. The cross section of 13000 barns corresponds to 157 displacements per electron with 16eV for the displacement threshold energy. In addition, P_e seems to have a finite value at ϕ_e=0. It would be attributable to the annealing effect of cascade regions caused by thermal and/or athermal migration of point defects, the latter of which would be caused by ion irradiation itself.

Irradiation with 1MeV electrons nucleates dislocation loops in Si and Ge at room temperature [133-136]. The final experiment in this chapter is designed to observe the nucleation process of dislocation loops under the accumulation of cascades. A focused 1MeV electron beam and a 30keV Xe^+ ion beam were simultaneously irradiated to Si and Ge. The electron dose rate of the focussed beam showed a Gaussian distribution, while the ions distribute homogeneously. **Figure 5.10** shows weak-beam dark-field micrographs of Si taken at and around the center of electron beam after irradiation for 600 sec with the maximum 1MeV electron dose rate of 4.8×10^{23} e/m^{2}s and 30keV Xe^+ ions of 1.0×10^{16} ions/m^{2}s. The micrographs (a), (b) and (c) in the figure show the area about 0, 1.5 and 3.6μm away from the center of electron beam, respectively. One can see higher density of dislocation loops and lower density

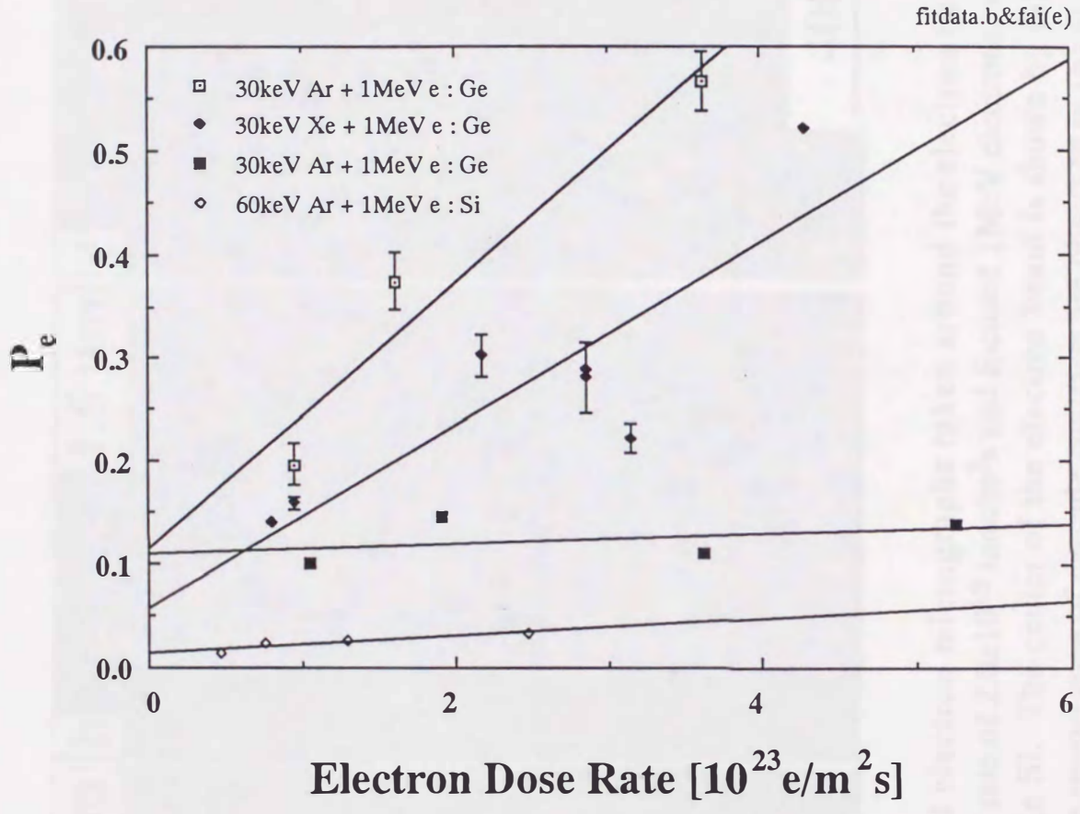

Figure 5.9 Values of theoretically-estimated electron dose rate, P_e, plotted against experimental one for various irradiation conditions.

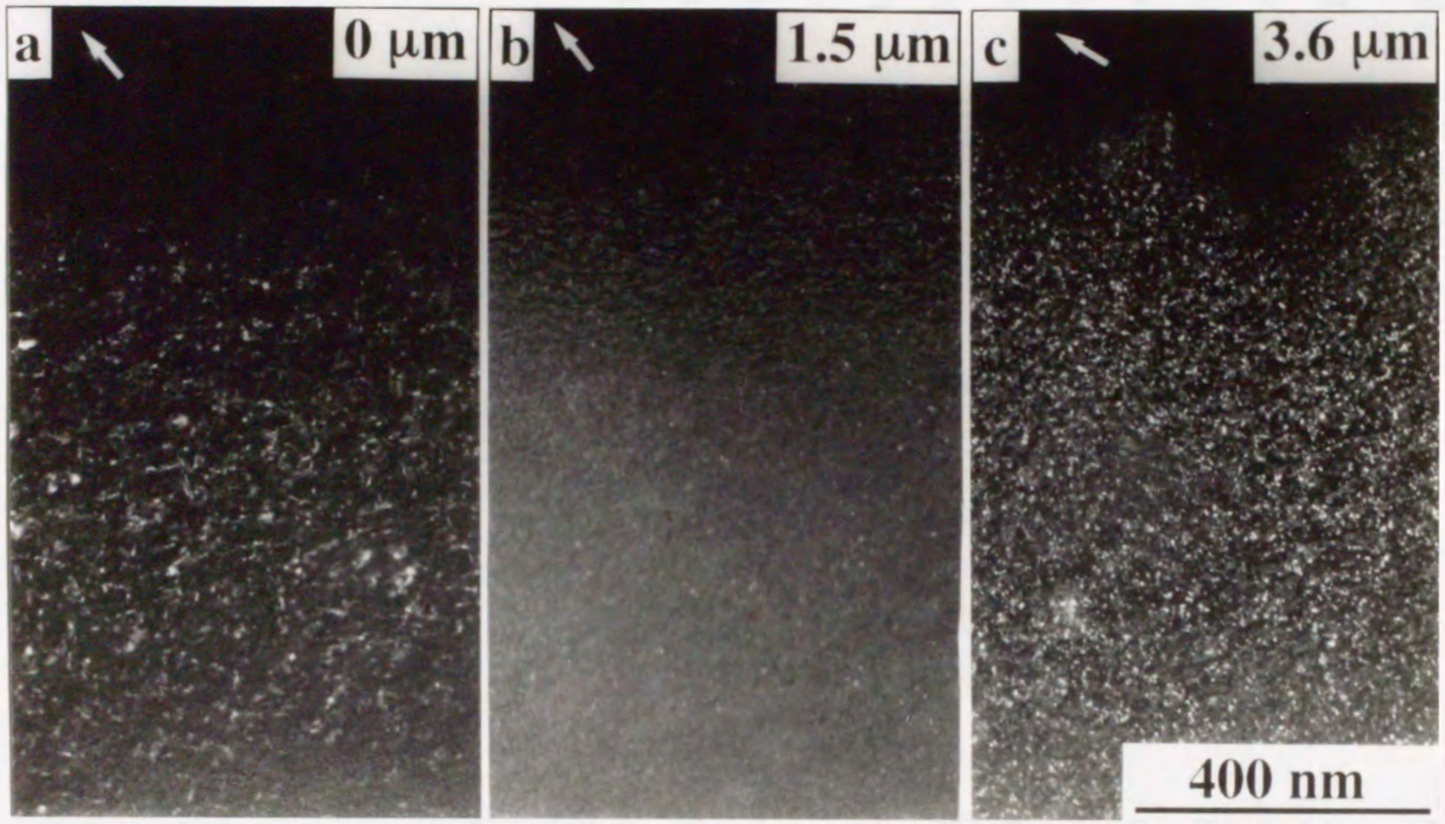

Figure 5.10 Weak-beam dark-field electron micrographs taken around the electron beam after dual-beam irradiation with a 30keV Xe^+ ion dose rate of $2.0x10^{15}$ ions/m^2s and focused 1MeV electrons, whose dose rate at the center is $2.9x10^{23}$ e/m^2s, for 2700s in Si. The center of the electron beam is shown by (a) where both cascade contrasts and loops are observed. The sparse zone of cascade contrasts are observed in (b) at the periphery of the electron beam. The density of cascade contrasts increases with increasing the distance from the center of the electron beam, as shown in (c). The arrows in the micrographs indicate **g**=220.

of cascade contrasts in (a), relatively low density of cascade contrasts in (b) and higher density of cascade contrasts in (c).

The area density of clusters which includes cascade contrasts and dislocation loops was traced and it is shown in **figure 5.11** as a function of the distance from the center of the electron beam. The density decreases gradually with increasing the distance and again it increases outside the beam, forming a sparse zone around the electron beam. Most of these defect clusters within the beam are interstitial-type dislocation loops induced by 1MeV electrons. Therefore, electron irradiation induces dislocation loops while it annihilates cascade damages. The interstitial atoms generated within the electron beam are also enforced to migrate outward from the electron beam, and annihilate cascade damages to form the sparse zone around the electron beam. The interstitial atoms migrate rather long distance in contrast to ones in Cu [11].

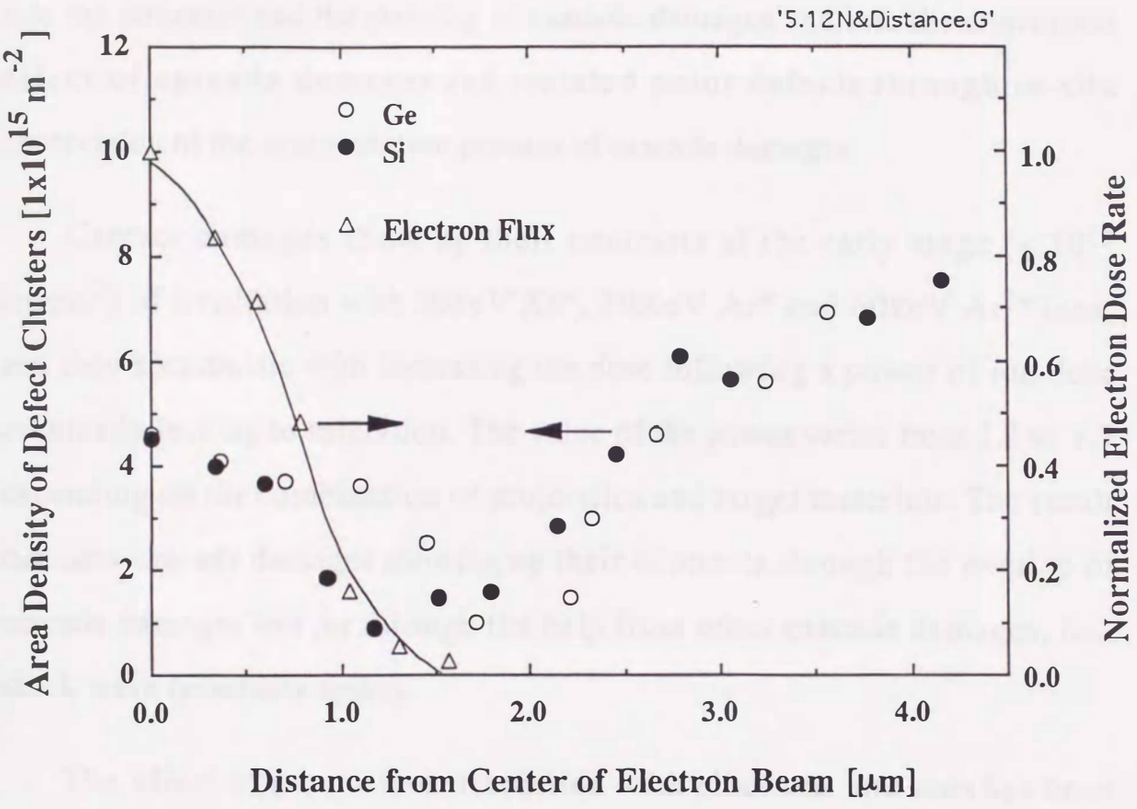

Figure 5.11 The area density of cascade contrasts and I-loops in Si and Ge produced by 30keV Xe^+ ions and a focused 1MeV electron beam as a function of the distance from the center of the electron beam. The irradiation was performed with an ion dose rate of $0.2x10^{16}$ and $1.0x10^{16}$ ions/m^2s for 2700s and 600s and with a focused electron beam, whose dose rates at the center are of $2.9x10^{23}$ and $4.8x10^{23}$ e/m^2s in Si and Ge, respectively.

5.5. CONCLUSIONS

The HVEM-ACC facility has been extensively used for getting insights into the structure and the stability of cascade damages and into the concurrent effect of cascade damages and isolated point defects through in-situ observation of the accumulation process of cascade damages.

Cascade damages show up their contrasts at the early stage (< 10^{15} ions/m^2) of irradiation with 30keV Xe^+, 30KeV Ar^+ and 60keV Ar^{2+} ions, and they accumulate with increasing ion dose following a power of ion dose eventually leading to saturation. The value of the power varies from 1.2 to 1.7 depending on the combination of projectiles and target materials. The result indicates cascade damages showing up their contrasts through the overlap of cascade damages and /or through the help from other cascade damages, i.e., shock wave (plasticity spike).

The effect of concurrent irradiation with electrons and ions has been realized as the retardation of the accumulation of cascade contrasts. Some of cascade contrasts disappear under continuous irradiation through their shrinkage without any structural change like loop formation. The area density eventually saturates and the saturated density decreases with increasing the electron dose rate.

Kinetic equations have been proposed with models in which cascade damages show up their contrasts through overlaps or help of other cascades and electron irradiation eliminates the visible (amorphous) region. The observed phenomena are well described with the model.

Heavy irradiation with ions and electrons induces dislocation loops through the nucleation and growth process. A sparse zone is formed around the electron beam, showing a rather long distant migration of interstitial atoms to annihilate cascade regions.

CHAPTER 6

EFFECT OF CONCURRENT ELECTRON IRRADIATION ON ION- INDUCED AMORPHIZATION IN SILICON

6.1. INTRODUCTION

The concurrent effect of dual-beam irradiation with ions and electrons on the accumulation process of amorphous regions induced by cascade damages has been discussed in the previous chapter in relatively low ion dose regions. In this chapter, the concurrent irradiation with fast electrons (0.1~1MeV) and high energy ions (~MeV) in rather high ion dose regions is studied. High energy ions generate cascades comprising of subcascades. The structure of subcascades is described as vacancy-rich cores surrounded by interstitial atoms, and the energy density of them is high (~1eV/atom). Therefore, in the following, the effect of subcascade is examined. As reviewed in **chapter 1**, ion irradiation induces amorphization in Si [34-38]. The critical dose for the amorphization depends on ion mass, energy, dose rate and temperature [137-139]. Alternatively, fast electrons induce no amorphous phase in Si even at 15K up to dose of several displacements per atom (dpa) [140,141]. The mechanism of the amorphization is, therefore, considered as the accumulation and overlaps of cascade damages. High energy ions produce relatively high energy PKAs. They generate several regions expressed as vacancy-rich cores surrounded by interstitials within cascades. Therefore, subcascades have an important role for the ion-induced amorphization. The concurrent effect of

dual-beam irradiation with ions and electrons was first observed in Si at 15K [28], and was realized as the prevention of ion-induced amorphization under the dual-beam irradiation. However, the systematic experiments have been required to get quantitative insight into the mechanism of the prevention effect.

Two objectives lie in this chapter. One is to clarify the mechanism of the ion-induced amorphization in terms of subcascades. Another one is to get insights into the concurrent effect on the ion-induced amorphization under irradiation with ions and electrons through the systematic experiments as functions of ion species, ion energy, ion dose rate and electron energy.

6.2. EXPERIMENTAL METHODS

Silicon transparencies were irradiated with ions and electrons in the HVEM-Tandem facility at ANL [5-9] under various conditions. All the experiments were done at room temperature, where interstitials and neutral and doubly charged vacancies were mobile. Irradiation with 0.4~1.5MeV Xe^+, Kr^+ and Ar^+ ions was carried out at ~10 degrees away from the foil normal being parallel to the <110> direction. Electron micrographs were taken mainly at the [110] pole, so that the electron beam was almost perpendicular to the specimen surface. Dual-beam irradiation was performed with a homogeneous ion beam and a focused electron beam showing the Gaussian distribution [142]. However, the electron beam is the ellipse in shape on films because of tilting the specimen during irradiation with ions and electrons and

of the intrinsic astigmatism of electron beam in the HVEM. Therefore, the diameter was measured along the tilt axis of the specimen, which was almost corresponding to the minor axis. The specimen thickness was adopted to be smaller than the range of ions so that most of ions penetrated the specimen.

6.3. ION-INDUCED AMORPHIZATION

Silicon transparencies were amorphized during irradiation with various kinds of ions as shown in **table 6.1** at room temperature. The critical ion dose for amorphization is listed in the table together with the critical damage in unit of dpa based on the formation of isolated Frenkel defects or cascade damages. The critical damage for amorphization was calculated using the TRIM-90 code with the displacement threshold energy of 16eV [143]. The last column shows the critical damage for amorphization on the assumption that only cascades or subcascades with energy larger than 15keV induce amorphous regions. As obviously seen in **table 6.1**, the critical damage for amorphization depends on ion species; that is, the more critical damage for amorphization is required for the specimen irradiated with the lighter ions under the assumption that the amorphization is induced by isolated point defects. Actually, however, high energy ions used for the experiments generate subcascades. A subcascade is a molten zone during its thermal spike [77]. The distorted lattice, then, undergoes a rearrangement to accommodate these defects as amorphous phase [83,84]. The stability of the amorphous phase depends on ion species and their energy, both of which are strongly related with the energy density of subcascades. Therefore, the effect of subcascades on the amorphization should be taken into account to explain the result in the table. The heavier ions deposit the more energy in a subcascade and result in amorphization with the less dpa. On the contrary, the lighter ions induce isolated point defects and their athermal migration other than cascades. The isolated point defects and their athermal migration contributes to the

Table 6.1 The critical ion dose for amorphization of Si irradiated with various kinds of ions. The critical ion dose is converted to dpa's based on isolated Frenkel pairs with 16eV for the displacement threshold energy and on subcascades with 15keV for the critical subcascade energy. The TRIM-90 code was used for the calculations.

Ions	Critical ion dose [ions/m^2]	Critical damage for amorphization [dpa]	Critical damage for amorphization due to 15keV subcascades [dpa]
1MeV Ar^+	$1.4x10^{20}$	9.1	0.69
0.4MeV Ar^+	$3.4x10^{19}$	4.4	0.32
1MeV Kr^+	$1.0x10^{19}$	3.3	0.28
1MeV Kr^+	$1.0x10^{19}$	2.8	0.27
0.8MeV Kr^{2+}	$6.7x10^{18}$	2.2	0.20
1.5MeV Xe^+	$5.0x10^{18}$	2.3	0.26
1MeV Xe^+	$3.3x10^{18}$	1.8	0.17

annihilation of the amorphous phase. As a result, heavier ions tend to induce more stable amorphous phase.

As emphasized in the previous section, the ion-induced amorphization undergoes through the accumulation of subcascades. Therefore, the threshold energy for subcascades is one of the important parameters for describing the ion-induced amorphization. Heinisch and Singh [144] have estimated the threshold energy for subcascades using the MARLOWE code [145] which provides reasonable simulation of displacement spikes based on a binary collision approximation taking into account the crystal structure. **Figure 6.1** is an example of their calculations showing the vacancy density in a cascade damage as a function of PKA energy. The vacancy density decreases as increasing PKA energy, showing a break point designated as the break-up energy at 23keV for Cu. The break-up energy is thought to be corresponding to onset of the production of subcascades, indicating a distinct change in the nature of the cascade damage. The TRIM-90 code also gives estimation of the threshold energy of subcascade formation, though it takes into account no definitive crystal structures. The estimation with the TRIM-90 code is compared with that through the MARLOWE code in **figure 6.1**. The threshold energy for subcascade formation is about 20keV for Cu, which is close to the result based on the MARLOWE code. The value of the threshold energy for subcascade formation in Si is estimated to be 15keV. The density of vacancies in 15keV subcascades in Si is calculated to be 1.3×10^{-3} vacancies/A^3, which corresponds to the energy density of about 0.4 eV/atom in a subcascade. This value is quite consistent with Howe's estimation based on experiments [89].

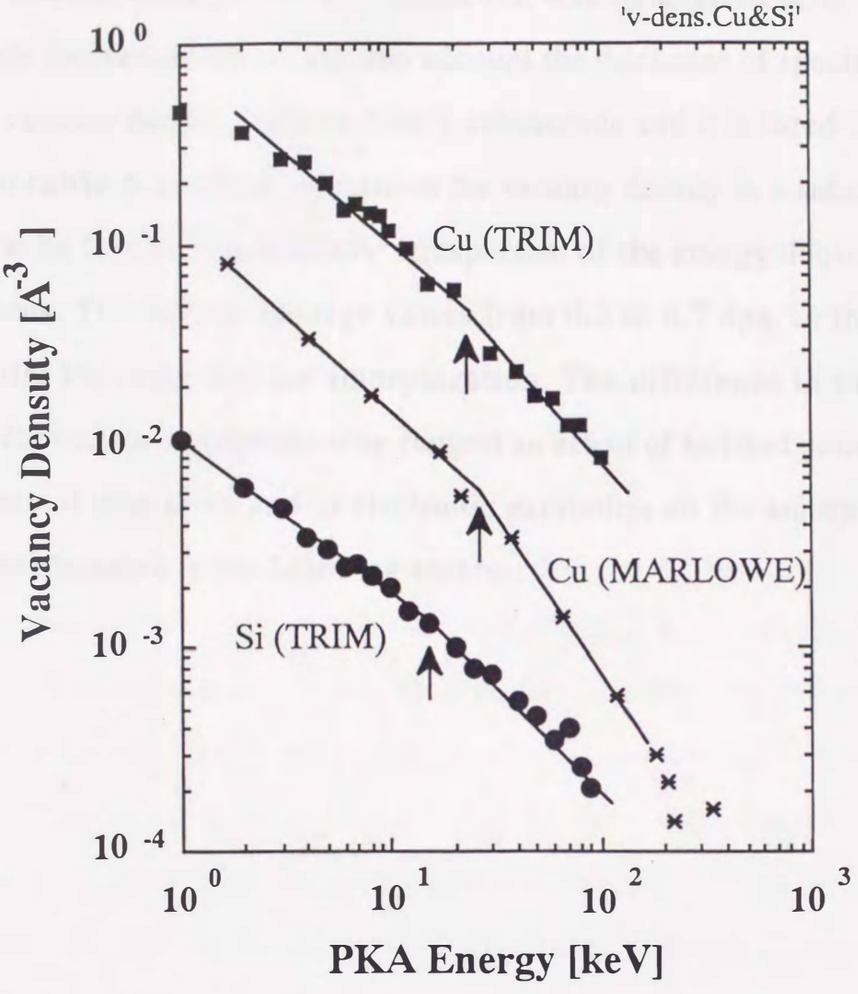

Figure 6.1 The average density of vacancies within an individual cascade in Cu and Si as a function of PKA energy calculated with the TRIM-90 code. Also shown in the figure is the average density of vacancies in the rectangular parallelepipeds enclosing cascades in Cu calculated by Heinisch and Singh [145]. The change in slopes indicates the threshold for the production of subcascades.

The critical damage for amorphization was calculated both from the subcascade formation rate taking into account the thickness of specimens and from the vacancy density within a 15keV subcascade and it is listed in the last column of **table 6.1**. In this calculation the vacancy density in a subcascade is assumed to be 1.3×10^{-3} vacancies/A^3 irrespective of the energy density within subcascades. The critical damage varies from 0.2 to 0.7 dpa, or the lighter ions require the more dpa for amorphization. The difference in the critical damages for various ion species may suggest an effect of isolated point defects, their athermal migration and/or electronic excitation on the amorphization, and will be discussed in the following section.

6.4. EFFECT OF CONCURRENT ELECTRON IRRADIATION ON ION-INDUCED AMORPHIZATION

It was first observed by Seidman et al. [28] that simultaneous irradiation with electrons prevented ion-induced amorphization. Stimulated by their findings, the dual-beam irradiation with ions and electrons has been extensively performed to clarify their concurrent effect on irradiation-induced amorphization. **Figure 6.2** shows a sequential change in microstructural evolution under dual-beam irradiation with 1.5MeV Xe^+ ions and a focused 1MeV electron beam. The outside region of the electron beam becomes amorphous, forming the interface of the amorphous region and the crystalline region inside the electron beam. A concurrent effect of electron irradiation is clearly seen as retardation or prevention of the ion-induced amorphization. The diameter of the crystal region is plotted as functions of the ion dose and the ion dose rate under irradiation with 1.5MeV Xe^+ ions and a focused 1MeV electron beam in **figure 6.3**. The diameter decreases and reaches a constant value with increasing ion dose. The saturation value of the diameter depends on the ion dose rate, being smaller with increasing it. The whole region even inside the electron beam became amorphous phase under irradiation with higher dose rates than 4×10^{16} ions/m^2s of 1.5MeV Xe^+ ions.

The concurrent effect depends on both dose rates of electrons and ions. The electron dose rate near and outside the edge of the focused electron beam is not large enough to prevent the ion-induced amorphization. The electron dose rate at the interface between the crystalline and amorphous phases,

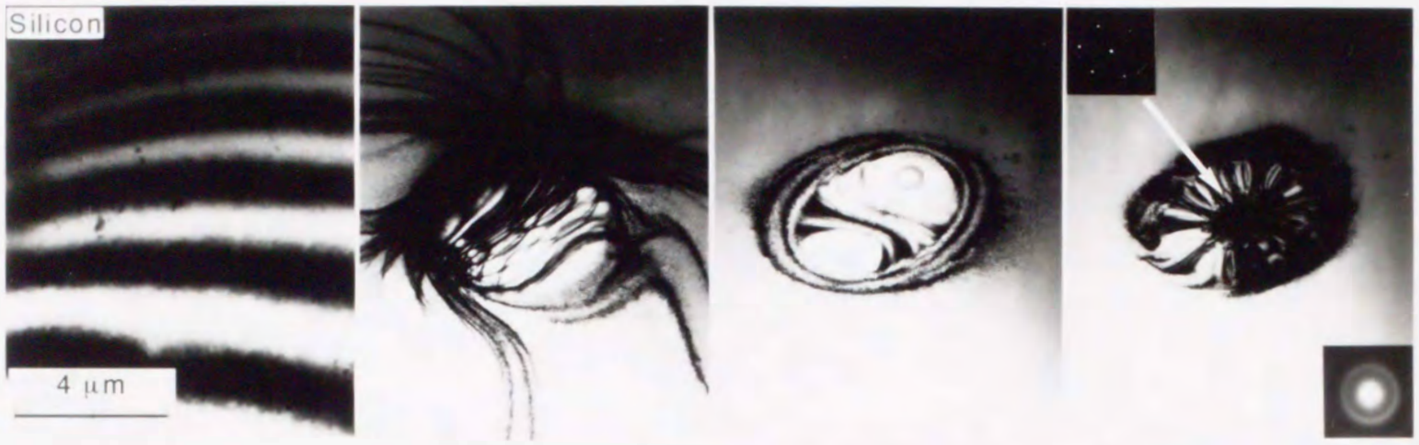

1MeV Kr^+ $\phi_i = 3.4 \times 10^{15}$ ions/m^2 s

500keV e^- $\phi_e^0 = 6.1 \times 10^{23}$ e/m^2 s

$\sigma_e = 0.77$ μm

Figure 6.2 A sequence of bright-field images showing retention of crystallinity inside the electron beam in Si under irradiation with 1MeV Kr^+ ions and a focused 500keV electron beam. The ion dose rate (ϕ_i) and the maximum dose rate (ϕ_c^0) or the standard deviation (σ_e) of the focused electron beam are shown in the figure.

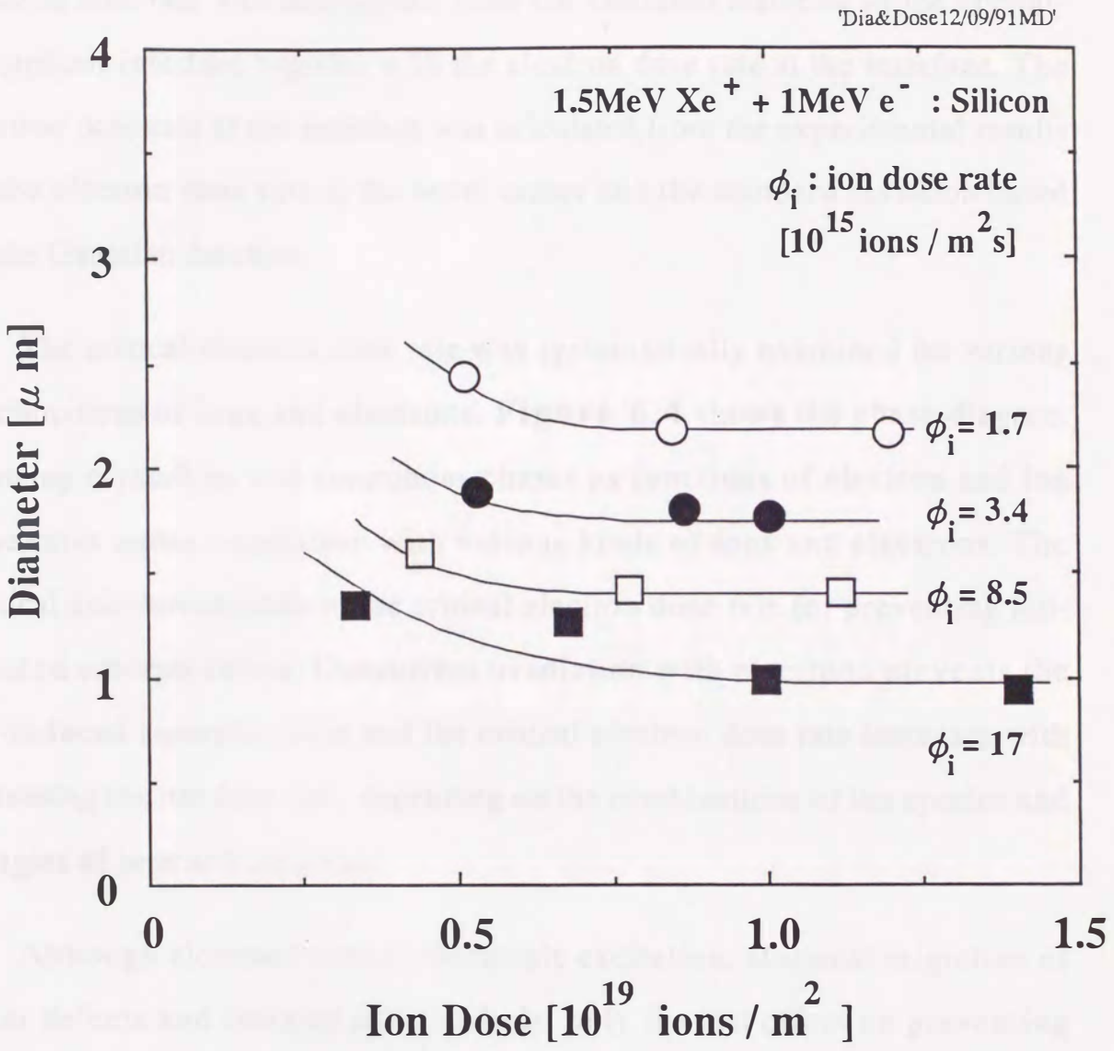

Figure 6.3 Change in diameter under irradiation with a focused electron beam and a 1.5MeV Xe^+ ion beam for various ion dose rates. The ion dose rate (ϕ_i) is shown in the figure and the maximum dose rate and the standard deviation of the electron beam are, respectively, 5.2×10^{23} e/m^{2}s and 0.6μm.

therefore, corresponds to the critical value enough to prevent ion-induced amorphization and is designated as the critical electron dose rate. The critical electron dose rate was determined from the saturated diameter of the crystal-amorphous interface together with the electron dose rate at the interface. The electron dose rate at the interface was calculated from the experimental results on the electron dose rate at the beam center and the standard deviation based on the Gaussian function.

The critical electron dose rate was systematically examined for various combinations of ions and electrons. **Figure 6.4** shows the phase diagram showing crystalline and amorphous phases as functions of electron and ion dose rates under irradiation with various kinds of ions and electrons. The vertical axis corresponds to the critical electron dose rate for preventing ion-induced amorphization. Concurrent irradiation with electrons prevents the ion-induced amorphization and the critical electron dose rate increases with increasing the ion dose rate, depending on the combinations of ion species and energies of ions and electrons.

Although electrons induce electronic excitation, athermal migration of point defects and isolated point defects, only the last effect on preventing amorphization is taken into consideration first. The horizontal and vertical axes in **figure 6.4** are converted into the damage rates in a unit of dpa/s, as shown in **figure 6.5**, based on the formation of Frenkel pairs. There are some trends for the relation between the damage rates induced by electrons and ions. The critical electron damage rate increases with increasing the ion dose rate, depending on ion species less than 5×10^{-3} dpa/s and converging the dependence of ion species higher than 5×10^{-3} dpa/s. The critical electron

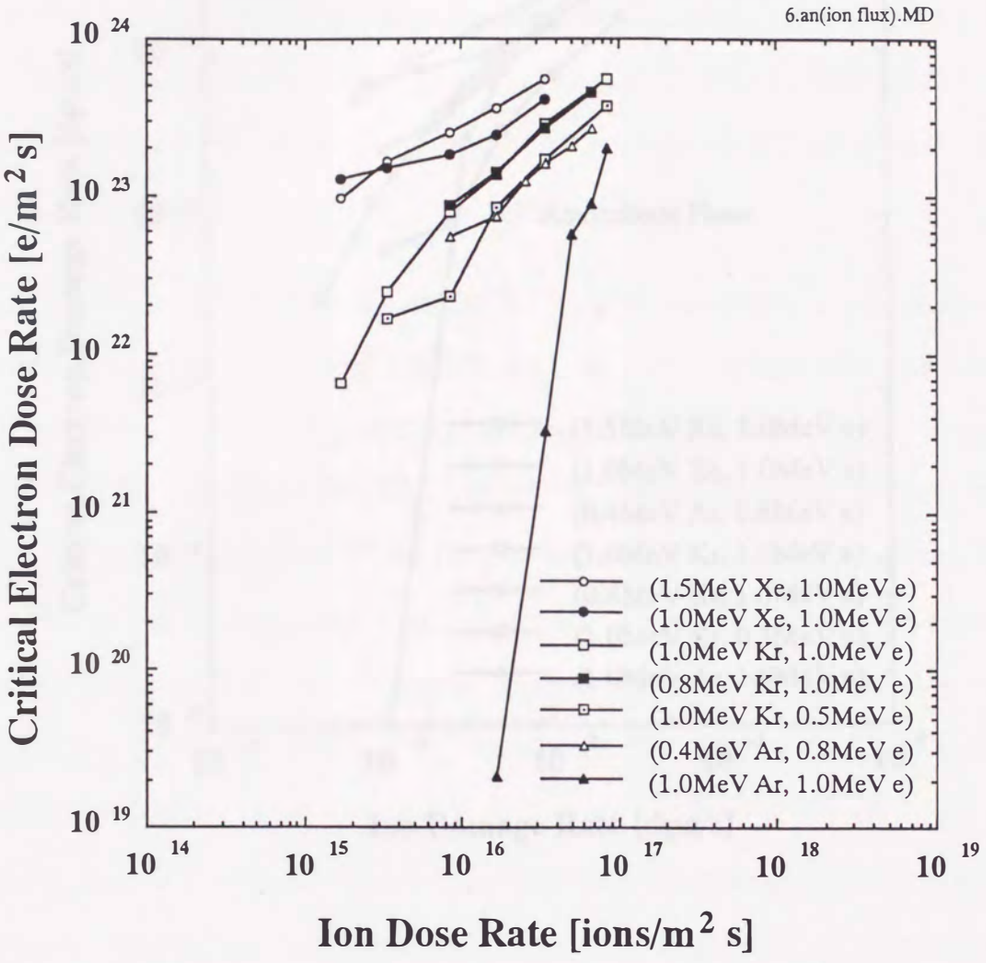

Figure 6.4 A phase diagram of crystal and amorphous phases in silicon in terms of critical electron dose rate and ion dose rate for various irradiation conditions.

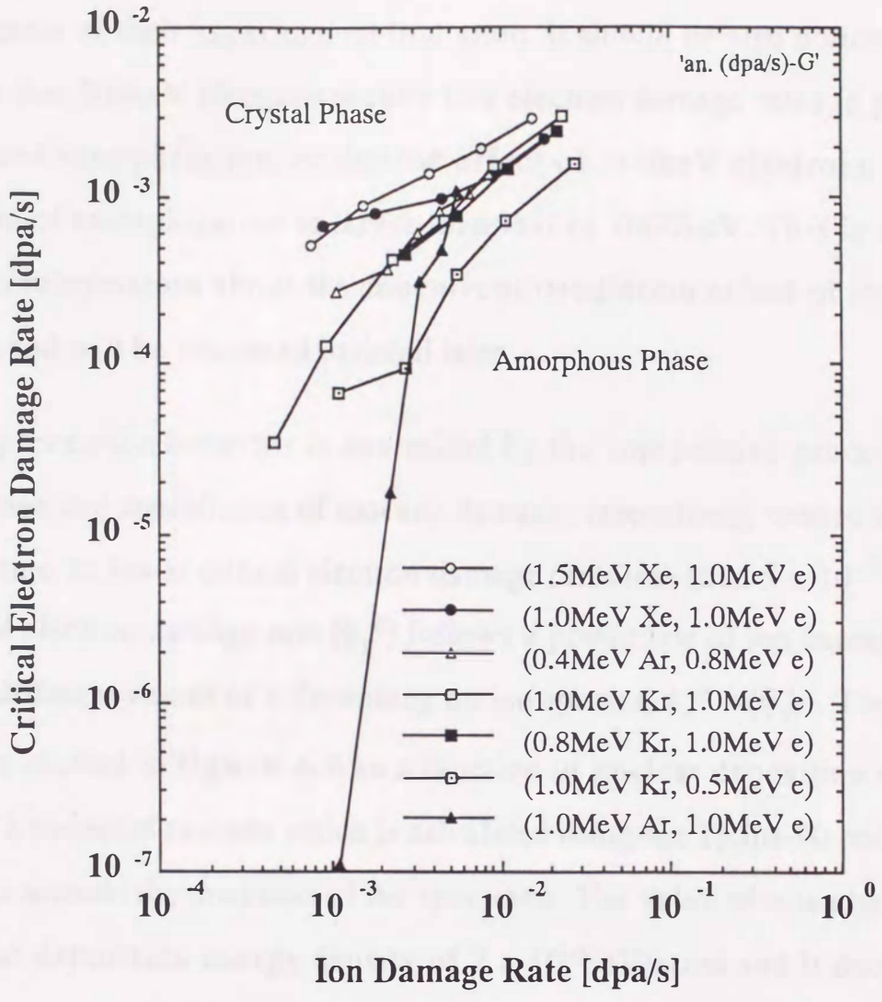

Figure 6.5 A phase diagram of crystal and amorphous phases in silicon in terms of critical electron damage rate and ion damage rate for various irradiation conditions. The damage rates are calculated based on the Frenkel pair formation with 16eV for the displacement threshold energy. There are two trends for the relation in which the critical electron damage rate depends on ion species less than 4×10^{-3} dpa/s (stage I) and it only depends on ion damage rate (stage II).

damage rate was not determined in higher electron damage rates than 4×10^{-2} dpa/s because of their experimental limitation. It should be also noticed from the figure that 500keV electrons require less electron damage rates to prevent ion-induced amorphization, or that the effect of 500keV electrons on the prevention of amorphization is larger than that of 1000keV. This is also an important information about the concurrent irradiation effect of ions and electrons, and will be discussed in detail later.

The prevention behavior is controlled by the competitive processes of accumulation and annihilation of cascade damages respectively caused by ions and electrons. In lower critical electron damage rates less than 5×10^{-3} dpa/s, the critical electron damage rate (ϕ_e^c) follows a power law of ion damage rate (ϕ_i) with different values of x depending on ion species, $\phi_e^c \propto (\phi_i)^x$. Then, the power x is plotted in **figure 6.6** as a function of nuclear deposition energy density in a transport cascade which is calculated using the TRIM-90 code with taking into account the thickness of the specimen. The value of x is about 6 at the nuclear deposition energy density of 7×10^{-6} eV/atom and it decreases rapidly to reach a constant value with increasing the energy density higher than 2×10^{-4} eV/atom, suggesting that the overlapping effect of subcascades becomes more significant when the energy density is larger than 2×10^{-4} eV/atom. The accumulation of cascade damages is high enough in the range of higher energy density than 2×10^{-4} eV/atom that no difference among values of the power x can be seen irrespective of ion species and their energies. In the range of energy density less than 2×10^{-4} eV/atom, on the contrary, the annihilation process through isolated point defects and their athermal migration becomes significant.

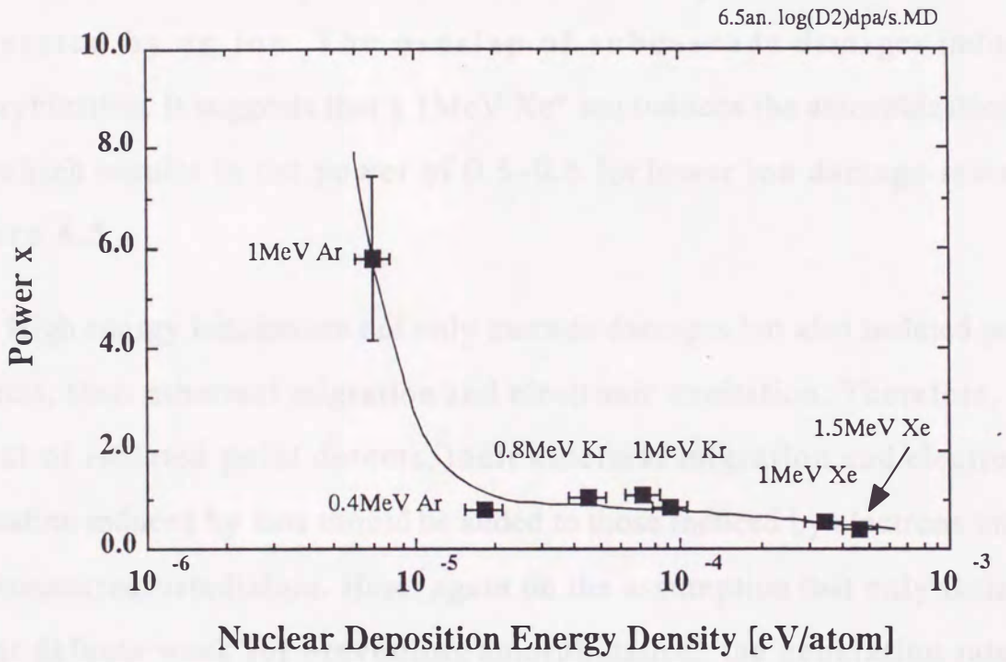

Figure 6.6 Plots of the power x in stage I, which is defined in figure 6.5, as a function of nuclear deposition energy density.

The formation probability of 15keV subcascade regions is estimated from the TRIM-90 code to be 0.6 and 5 for Si transparencies with thickness of 320 and 260nm experimentally used for irradiation with 1MeV Ar^+ and Xe^+ ions, respectively. The average distance of 15keV subcascade damages in Si, whose longitudinal and the radial ranges are 24 and 10nm, respectively, is estimated from the TRIM-90 code to be about 55nm for irradiation with a 1MeV Xe^+ ion. Therefore, the overlap of subcascade damages is possible within a cascade generated by an ion. The overlap of subcascade damages induces amorphization. It suggests that a 1MeV Xe^+ ion induces the amorphization in Si, which results in the power of 0.5~0.6 for lower ion damage rates in **figure 6.5**.

High energy ions induce not only cascade damages but also isolated point defects, their athermal migration and electronic excitation. Therefore, the effect of isolated point defects, their athermal migration and electronic excitation induced by ions should be added to those induced by electrons under the concurrent irradiation. Here, again on the assumption that only isolated point defects work for preventing amorphization, the generation rate of isolated point defects both by electrons and ions is estimated by using the NRT model. **Figure 6.7** shows the damage rate for preventing amorphization through isolated point defects as a function of damage rate for amorphization due to subcascades with energies higher than 15keV. The collisional cross sections of producing isolated point defects and subcascades were calculated using Lindhard theory. The damage rate for preventing amorphization is almost linearly proportional to the damage rate for amorphization except for

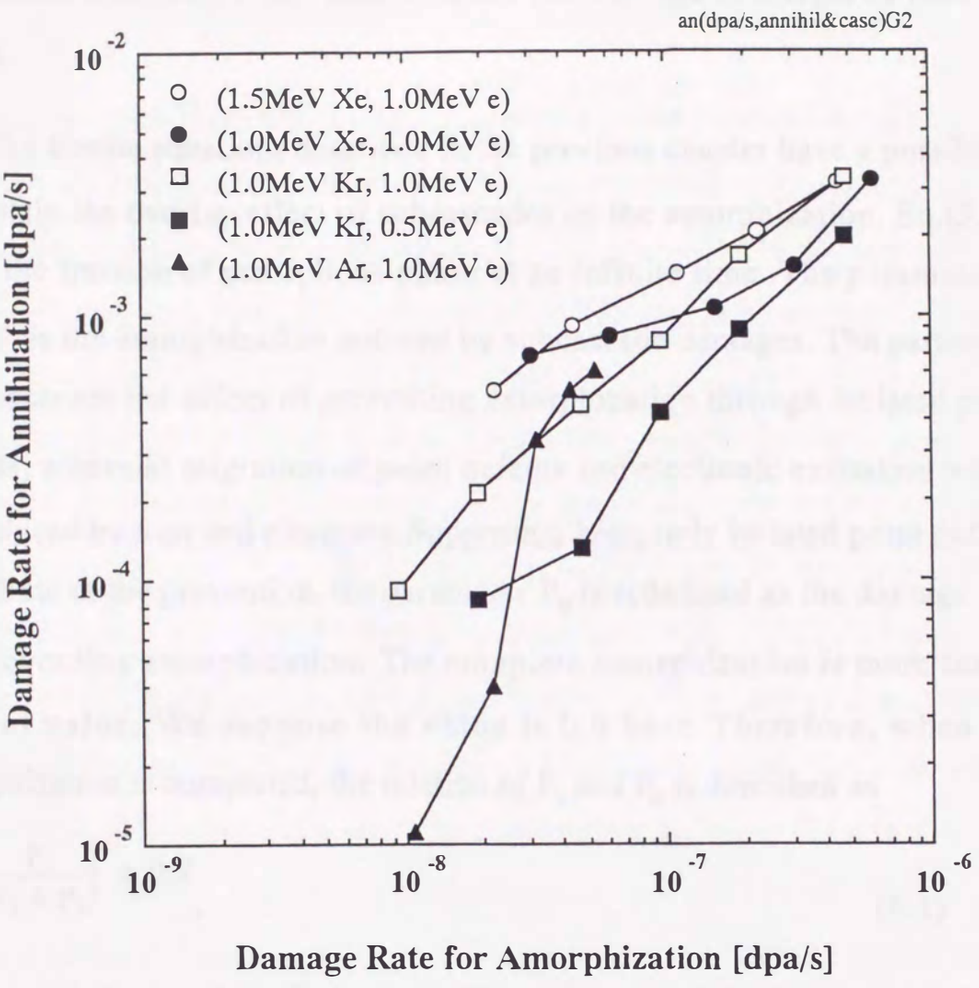

Figure 6.7 The ion and electron damage rates for preventing amorphization as a function of the ion damage rates for amorphization. The ion and electron damage rates for preventing amorphization are based on Frenkel pair formation with 16eV for the displacement threshold energy and those for amorphization are based on subcascade formation with 15keV for critical subcascade energy.

irradiation with 1MeV Ar^+ ions at lower ion damage rate regions ($\leq 3\times10^{-8}$ dpa/s).

The kinetic equations described in the previous chapter have a possibility to explain the overlap effect of subcascades on the amorphization. Eq.(5.11) gives the fraction of amorphous phase at an infinite time. The parameter P_i describes the amorphization induced by subcascade damages. The parameter P_e represents the effect of preventing amorphization through isolated point defects, athermal migration of point defects and electronic excitation which are induced by ions and electrons. Supposing, here, only isolated point defects contribute to the prevention, the parameter P_e is redefined as the damage rate for preventing amorphization. The complete amorphization is more than a critical value. We suppose the value is 0.9 here. Therefore, when the amorphization is completed, the relation of P_i and P_e is described as

$$\left(\frac{P_i}{P_i + P_e}\right)^n \geq 0.9 \quad , \tag{6.1}$$

where, n is the number of overlaps. The value of 0.9 itself is not a critical factor for the relation between P_i and P_e as can be seen in eq.(6.1). Hence, the dose rate for preventing amorphization is derived as

$$P_e^c = \left(0.9^{-1/n} - 1\right) P_i \quad . \tag{6.2}$$

Eq.(6.2) obviously indicates that the damage rate for preventing amorphization linearly increases with increasing that for amorphization. Therefore, the linear relationship in **figure 6.7** is quite reasonable. Eq.(6.2) also suggests that the critical electron dose rate decreases with increasing the number of subcascade overlaps. Therefore, in case of irradiation with 1MeV

Ar^+ ions, the more number of overlaps is required when the less ion dose rate is chosen.

Fast electrons interact with constituent atoms and induce isolated point defects, their athermal migration and electronic excitation, depending on the cross section for each interaction mechanism. In order to get information about the preventing mechanism of amorphization due to electron irradiation, the electron energy dependence of the critical electron dose rate was, then, further examined under dual-beam irradiation with ions and electrons. **Figure 6.8** shows typical examples of the microstructural evolution under dual-beam irradiation with 1MeV Kr^+ ions and 500keV electrons and with 400keV Ar^+ ions and 200keV electrons. Irradiation with 1MeV Kr^+ ions and a focused 500keV electron beam makes the clear interface between crystalline and amorphous regions as shown in **figure 6.8** (a). An example of dual-beam irradiation with less energetic electrons (200keV) is shown in **figure 6.8** (b). Same effect was also observed under concurrent irradiation with 400keV Ar^+ ions and 100keV electrons. Such low energy electrons displace almost no Si atoms with the threshold energy of 16eV. This obviously mentions that even lower energy electrons prevent the ion-induced amorphization. The prevention is presumably caused not only by generation of isolated point defects but also by athermal migration of point defects and electronic excitation.

The critical electron dose rate was further investigated as a function of electron energy under concurrent irradiation with 400keV Ar^+ ions and electrons, and the result is shown in **figure 6.9**. The critical electron dose rate increases with increasing electron energy, though experimental errors are

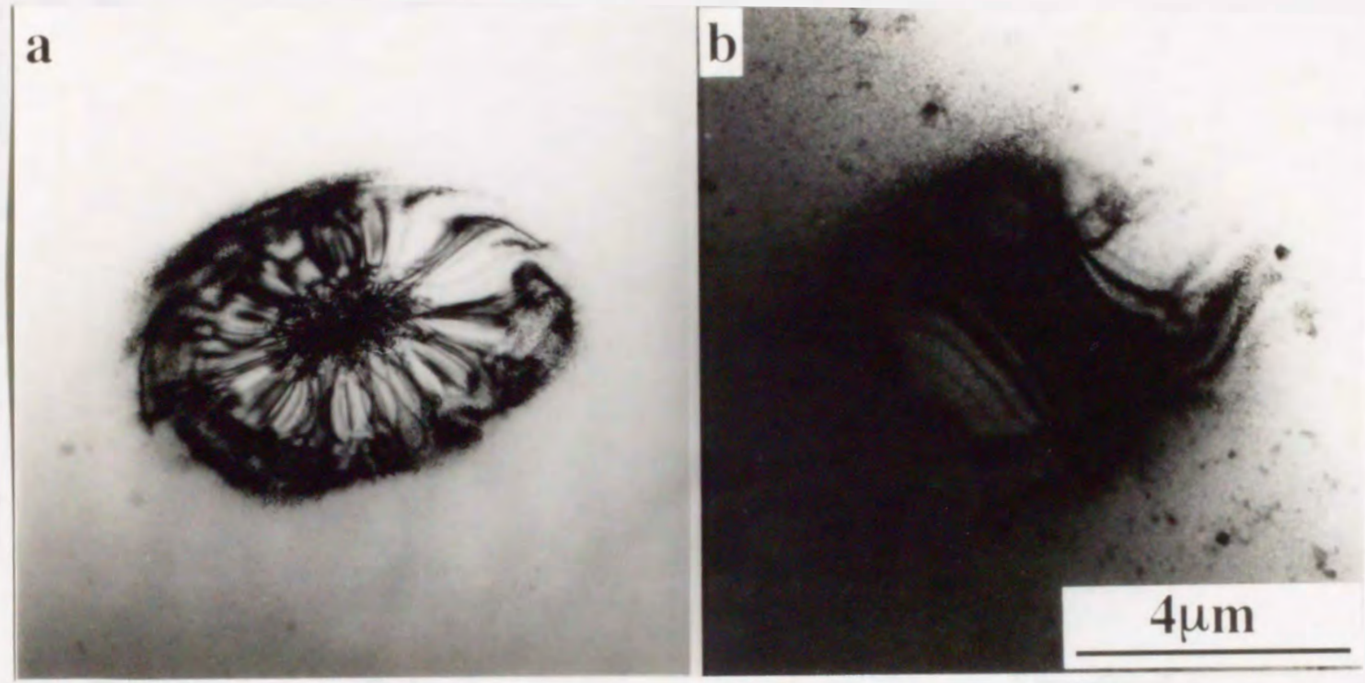

Figure 6.8 The micrographs showing the retardation effect under irradiation with (a) a 1MeV Kr^+ ion dose rate of $3.4x10^{15}$ ions/m^2s and a 500keV electron dose rate of $6.1x10^{23}$ e/m^2s for 5000s and with (b) a 400keV Ar^+ ion dose rate of $8.5x10^{15}$ ions/m^2s and 200keV electrons for 4000s. Clear interface of crystal and amorphous region is formed in (a) in contrast to that in (b). Small dot contrasts around the interface in (a) and (b) are thought crystalline region.

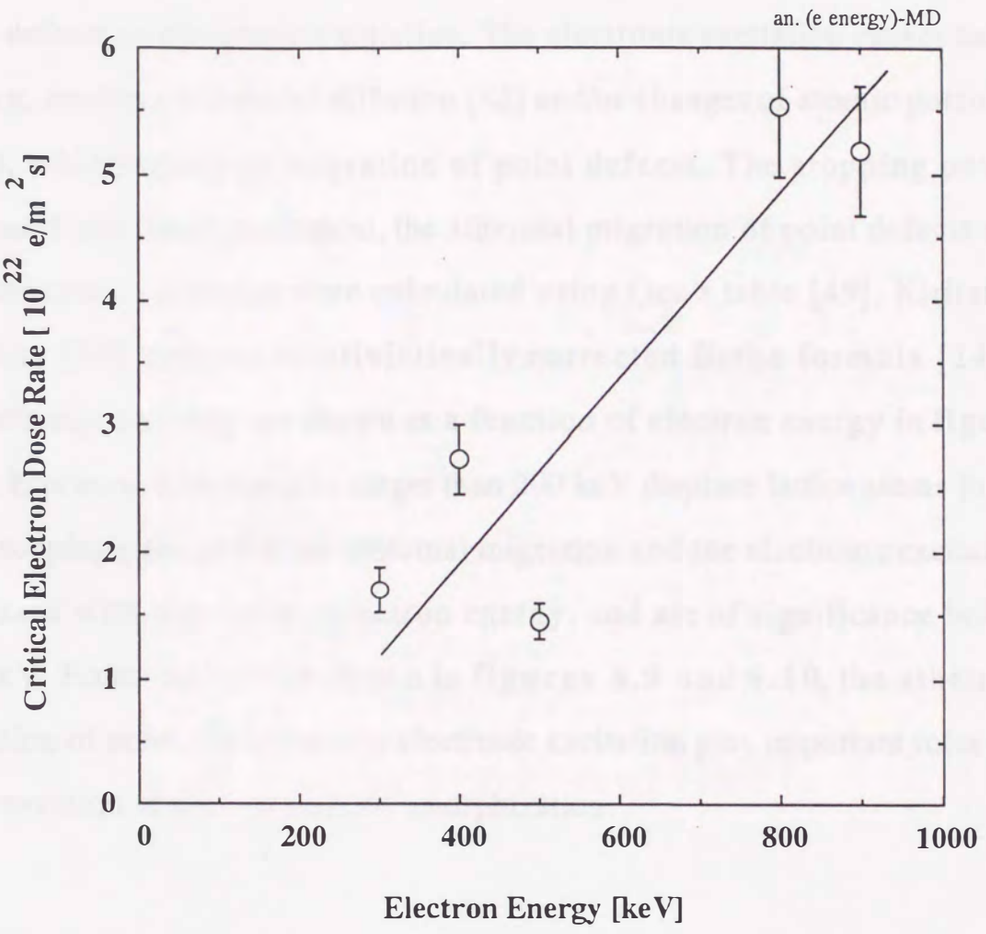

Figure 6.9 The electron energy dependence of the critical electron dose rate under irradiation with a 400keV Ar^+ dose rate of $8.5x10^{15}$ ions/m^2s and a focused electrons. The electron dose rates and the standard deviations are, respectively, $2\sim4x10^{23}$ e/m^2s and 0.5~1.0μm. As increasing electron energy, the critical electron dose rate increases, i.e., an electron with lower energy is more effective for the retardation.

large due to astigmatism of the electron beam; namely, electrons with the lower energy are the more effective for preventing ion-induced amorphization. Electrons having lower energies than 200keV mainly play roles in the annihilation of cascade damages through the athermal migration of point defects or electronic excitation. The electronic excitation causes beam heating, irradiation-induced diffusion [82] and/or changes of atomic potential [146], which result in migration of point defects. The stopping power dissipated into the displacement, the athermal migration of point defects and the electronic excitation were calculated using Oen's table [49], Kiritani's formula [50] and the relativistically corrected Bethe formula [147], respectively, and they are shown as a function of electron energy in **figure 6.10**. Electrons with energies larger than 200 keV displace lattice atoms in Si. The stopping powers for the athermal migration and the electronic excitation increases with decreasing electron energy, and are of significance below 200keV. From the results shown in **figures 6.9** and **6.10**, the athermal migration of point defects and/or electronic excitation play important roles for the prevention of the ion-induced amorphization.

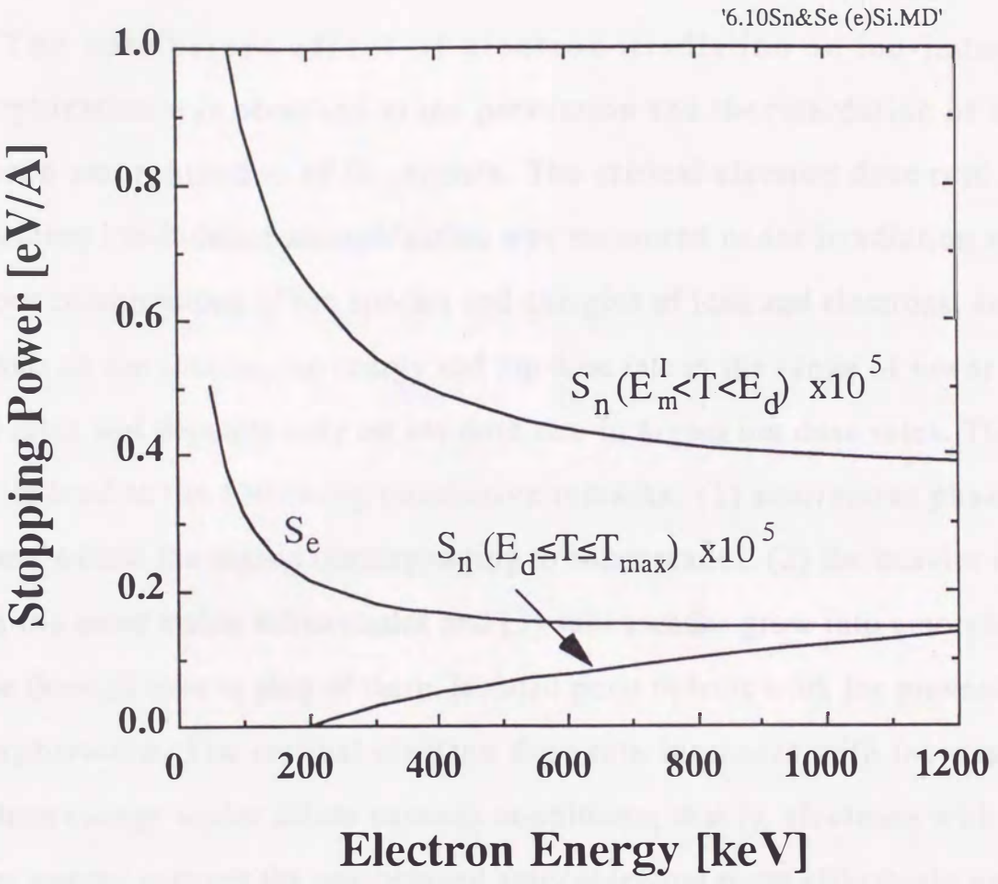

Figure 6.10 Nuclear and electronic stopping power as a function of electron energy. Nuclear stopping power, multiplied by a factor of 10^5, is described by two processes; one for displacements and another for athermal migration of point defects. The domain for integration is taken from displacement threshold energy for the former one, and from migration energy of interstitial atoms to the displacement threshold energy for the latter one.

6.5.CONCLUSIONS

The concurrent effect of electron irradiation on ion-induced amorphization was observed as the prevention and the retardation of ion-induced amorphization of Si crystals. The critical electron dose rate for preventing ion-induced amorphization was measured under irradiation with various combinations of ion species and energies of ions and electrons, and it depends on ion species, ion energy and ion dose rate in the range of lower ion dose rates and depends only on ion dose rate in higher ion dose rates. Those results lead to the following conclusive remarks; (1) amorphous phase is formed within the region corresponding to subcascades, (2) the heavier ions form the more stable subcascades and (3) subcascades grow into amorphous phase through overlapping of them. Isolated point defects work for preventing amorphization. The critical electron dose rate increases with increasing electron energy under dilute cascade conditions; that is, electrons with the lower energy prevent the ion-induced amorphization more effectively under those conditions. The prevention is, therefore, concluded to be mainly caused by the athermal migration of point defects and/or electronic excitation in addition to the isolated point defects.

CHAPTER 7

STABILITY OF CASCADE DAMAGES IN GERMANIUM

7.1. INTRODUCTION

As revealed in **chapter 4**, the structure of cascade damages in Si and Ge is the amorphous phase surrounded by high concentration of point defects. The amorphous phase recrystallizes at considerably lower temperatures between 300 and 500K, depending on energy density [89,90] during thermal annealing in contrast to the temperature (~840K) at which the epitaxial regrowth of amorphous layer takes place onto an underlying crystalline layer [148]. Overlapped regions of cascade damages, which are caused by the irradiation with higher ion dose [149] and by the irradiation with molecular ions [89,90], tend to form more stable amorphous regions against thermal annealing. The annealing behavior of cascade damages induced by 80 and 118keV Bi^+ ions [89,90] shows two stages during isochronal annealing; there are the recovery stage of disordered regions at ~400K and the recrystallization stage of amorphous regions at ~500K. Hypotheses are that disordered regions have an important role for the annealing behavior, and that the high dense energy deposition and the heavy irradiation attribute to the formation of dense overlaps of subcascades resulting in the growth of amorphous phase.

In this chapter, the annealing behavior of cascade damages in Ge irradiated with 30keV Xe^+ ions will be further investigated under electron

irradiation and isochronal annealing. The relation between the stability and the structure of cascade damages will be deduced through the discussion on the annealing mechanism of cascade damages under irradiation and thermal annealing.

7.2. EXPERIMENTAL METHODS

The first step of experiments was to irradiate Ge with 20 and 30keV Xe^+ ions of the order of 10^{16} ions/m^2 at room temperature, which induce no overlap of cascade damages. The irradiated specimens were, then, subjected to either electron irradiation or isochronal annealing in the HVEM. In-situ observation was performed under electron irradiation and isochronal annealing, and the cascade density was measured as functions of irradiation time, electron energy, electron dose rate and observation conditions such as the diffraction vector **g** and the deviation parameter **s**. Observation was always performed under the condition that **g**=220 and $|\mathbf{s}|=4\sim5\times10^{-3}$ A^{-1}, except for experiments on the (**g**,**s**) dependence. The isochronal annealing was carried out from room temperature to 673K with the average increasing rate of about 0.008K/s for specimens irradiated with 20keV Xe^+ ions.

7.3. RESULTS AND DISCUSSION

Figure 7.1 is a typical sequence showing the annihilation of cascade damages during irradiation with a 750keV electron dose rate of 6.7×10^{22} e/m^{2}s. Some of cascade damages disappear during continuous electron irradiation through the shrinkage of their contrasts without any structural change such as loop formation. The number of cascade contrasts decreases with increasing electron irradiation time. The area density of cascade contrasts is adopted here as the density of cascade damages, because the range of 30keV Xe^+ ions in Ge is 12.9nm which is much smaller than the specimen thickness (about 100nm). **Figure 7.2** shows the annihilation of cascade contrasts under irradiation with 1MeV electron dose rates of 0.7, 2, 5 and 7×10^{23} e/m^{2}s. The density decreases exponentially with increasing irradiation time. From this result, a hypothesis may be drawn that each cascade damage annihilates by absorbing definite number of interstitial atoms. In the case of specimens whose surfaces act as dominant sinks for interstitial atoms and vacancies, interstitial atoms keep their concentration to be the constant value C_i^0 which is written as

$$C_i^0 = \frac{\sigma_d \phi}{M_i C_s}, \qquad (7.1)$$

where, σ_d is the displacement cross section of Ge, ϕ the electron dose rate, M_i the mobility of interstitial atoms and C_s the sink concentration of surface. The annihilation of cascade damages is based on the absorption of interstitial atoms, and its behavior is described by using eq.(5.10.a) without considering the ion irradiation term (P_i=0). New variables N and λ instead of C_A and P_e in eq.(5.10a) follow the equation

Figure 7.1 A sequence of weak-beam dark-field images showing annihilation of cascade contrasts under irradiation with a 750keV electron dose rate of 6.7×10^{22} e/m^{2}s. Cascade contrasts are previously induced by irradiation with a 30keV Xe^+ ion dose of ~10^{16} ions/m^2.

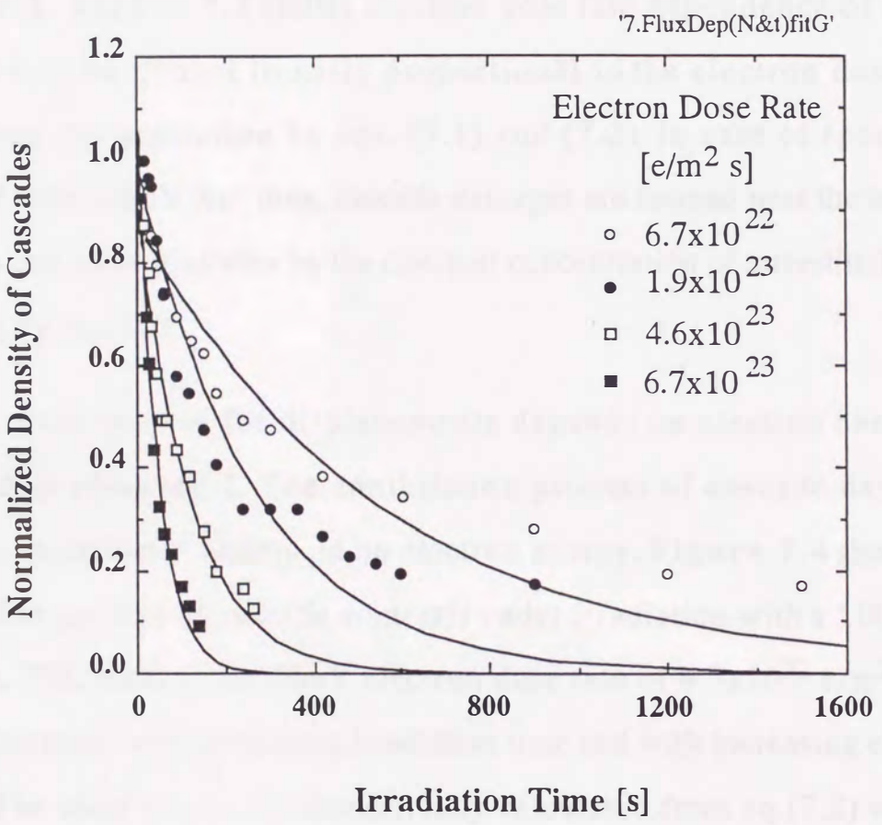

Figure 7.2 The annihilation process of cascade contrasts for various electron dose rates. The density of cascade contrasts is normalized by the density at the initial value. The solid curves are based on eq. (7.2) so as to fit to the experimental data.

$$\frac{dN}{dt} = -\lambda N \quad , \qquad (7.2)$$

where N, t and λ represent, respectively, the area density of cascade contrasts, electron irradiation time and the annihilation constant independent of t and proportional to C_i^0. Fitting curves derived from eq.(7.2) are also shown in **figure 7.2**. **Figure 7.3** shows electron dose rate dependence of λ, and indicates λ to be almost linearly proportional to the electron dose rate, confirming the prediction by eqs. (7.1) and (7.2). In case of specimens irradiated with 30keV Xe^+ ions, cascade damages are formed near the incident specimen and controlled also by the constant concentration of interstitial atoms described by eq.(7.1).

The cross section for displacements depends on electron energy as reviewed in **chapter 2**. The annihilation process of cascade damages, therefore, is expected to depend on electron energy. **Figure 7.4** shows the annihilation process of cascade contrasts under irradiation with a 100, 160, 200, 500, 750, 1000 or 1250keV electron dose rate of 6.7×10^{22} e/m^2s. The density decreases with increasing irradiation time and with increasing electron energy. The solid curves are theoretically calculated from eq.(7.2) with the value of λ so as to provide the best fit to the experimental results. The values of λ thus obtained are plotted in **figure 7.5** as a function of electron energy. The cross section for the atomic displacement in Si can be derived from the integration of eq.(2.15) with 16eV for the displacement threshold energy of Ge, showing the critical electron energy to produce displacements to be about 450keV. Non-trivial values below 450keV are not due to the atomic displacements but due to athermal migration of point defects. It is, therefore, hypothesized that the annihilation process of cascade contrasts is controlled by

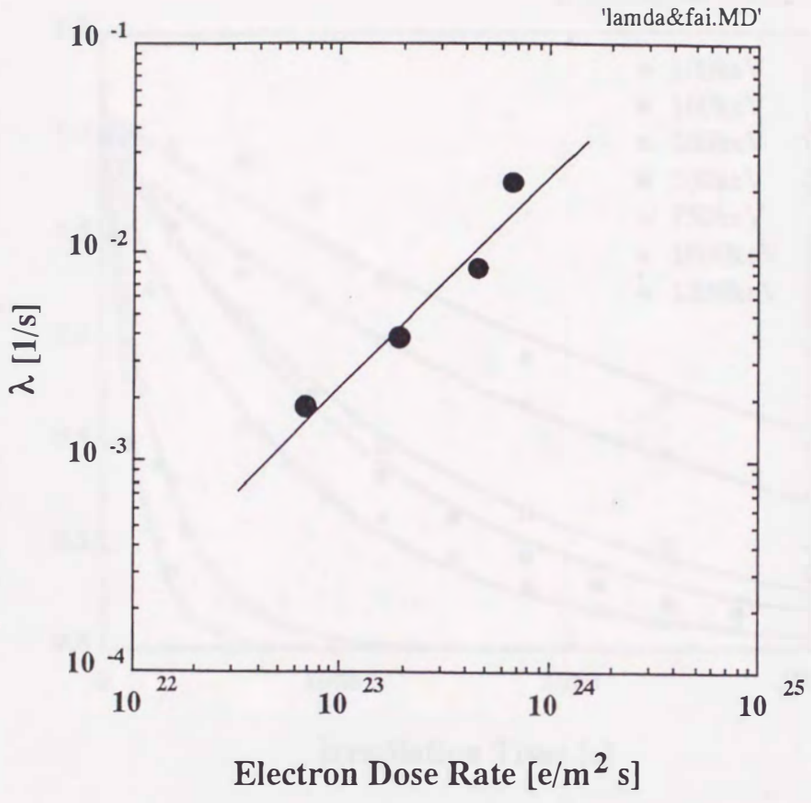

Figure 7.3 The annihilation constant of cascade contrasts, λ, as a function of electron dose rate.

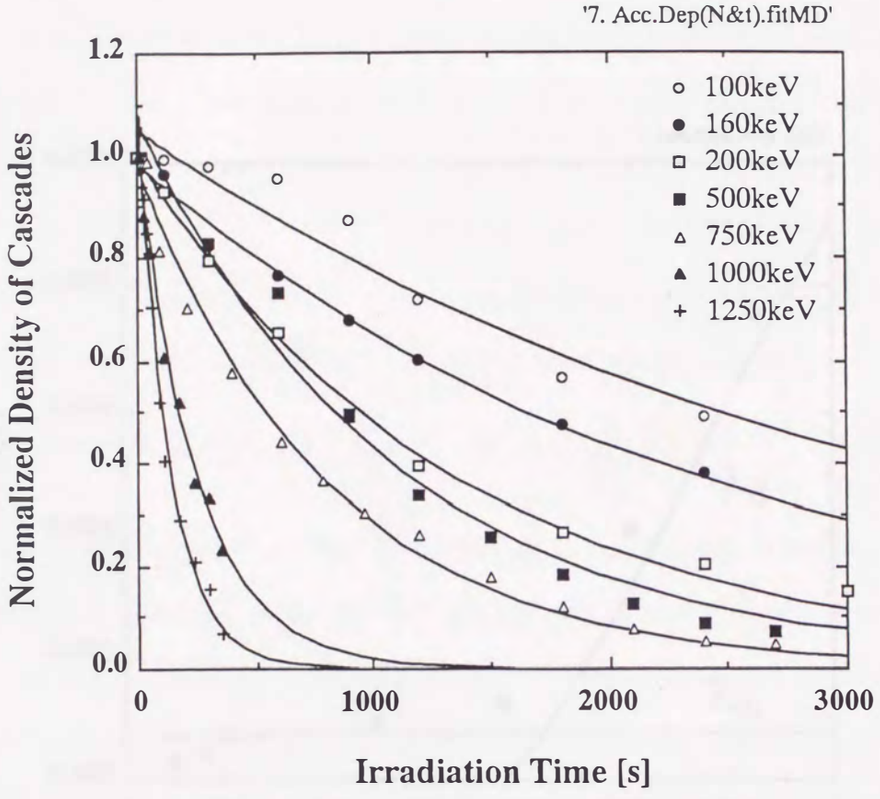

Figure 7.4 The annihilation process of cascade contrasts for various energies of electrons. The density of cascade contrasts is normalized by the density at the initial value. The solid curves are based on to eq. (7.2). Note that irradiation with 100, 160 and 200keV electrons induce no displacements of atoms, but annihilate cascade contrasts.

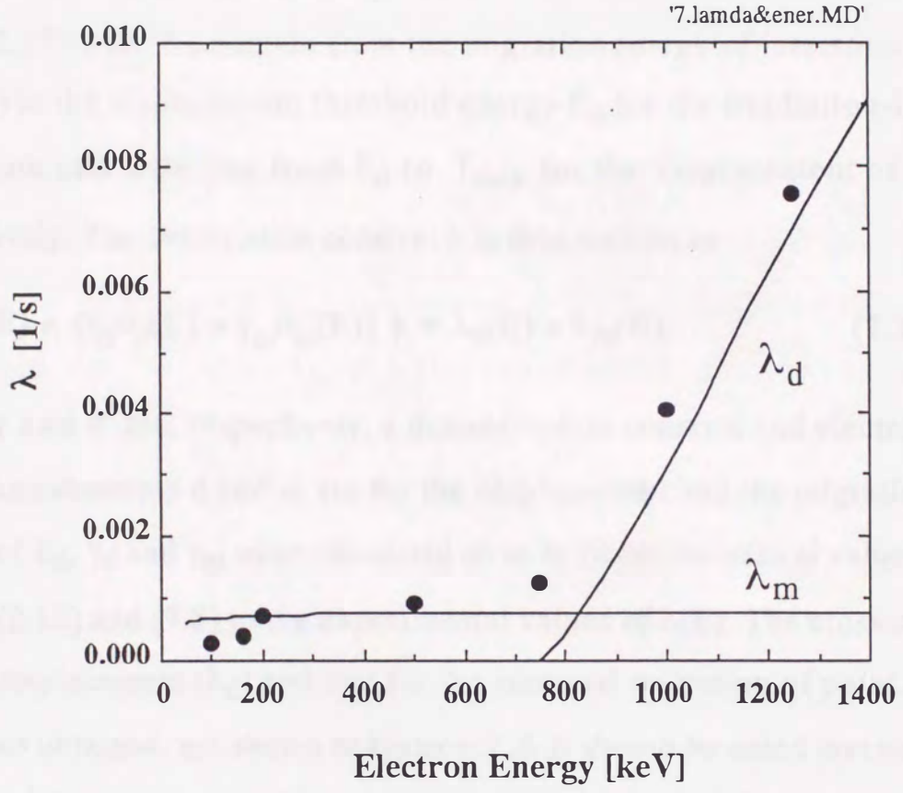

Figure 7.5 Annihilation constant of cascade contrasts, λ, as a function of energy of electrons. Solid curves are derived from eq. 7.3 based on the annihilation process controlled by the atomic displacement (λ_d) and the athermal migration of point defects (λ_m).

two kinds of irradiation processes; those are the displacement of atoms and the irradiation-induced migration of point defects. The reason the electronic excitation is not taken into account the annihilation process is that the value of λ is of trivia in contrast to the larger cross section below 100keV. Both of the cross sections for the irradiation processes were derived from the integration of eq.(2.15) with the domain from the migration energy of interstitial atoms (0.2eV) to the displacement threshold energy E_d for the irradiation-induced migration and with one from E_d to T_{max} for the displacement of atoms, respectively. The annihilation constant λ is then written as

$$\lambda(E) = \{\gamma_d \sigma_d(E) + \gamma_m \sigma_m(E)\}\ \phi \equiv \lambda_d(E) + \lambda_m(E), \qquad (7.3)$$

where γ and ϕ are, respectively, a dimensionless constant and electron dose rate. The subscripts d and m are for the displacement and the migration. The values of E_d, γ_d and γ_m were calculated so as to fit the theoretical values based on eqs.(2.18) and (7.3) to the experimental values of $\lambda(E)$. The cross sections for the displacement (λ_d) and that for the athermal migration of point defects (λ_m) thus obtained, are shown in **figure 7.5**. It should be noted that the value of E_d is determined to be 33eV which is about twice of the literature value [141]. The values for γ_d and γ_m are estimated as 8.2×10^{-3} and 1.2×10^{-7}, respectively. The physical meaning of γ is the efficiency of the contribution of each process to the annihilation of cascade damages.

As revealed in **chapter 6**, electrons with the lower energy are the more effective for preventing the ion-induced amorphization in contrast to the result in **figure 7.5**. The difference of these phenomena is caused based on the different experimental conditions, on is the concurrent irradiation with ions

and electrons and the other is post-irradiation with electrons after ion irradiation. During concurrent irradiation with electrons and ions, cascade damages, isolated point defects and irradiation-induced migration of point defects are introduced. The concurrent effects could be introduced under this condition. One possible concurrent effect is that isolated point defects are introduced by ions, and athermal migration and electronic excitation induce the diffusion of them.

The value of λ depends also on observation conditions which are described as **g** vector and deviation parameter **s**. The **g** and **s** dependences of λ are shown in **figure 7.6.** It can be seen in the figure that the lower index of **g** vector ascribes to the higher value of λ and that the value of λ depends on the value **s** except for **g**=111. In case of **g**=111, the value of λ at **s**=0 is quite larger than the others at different values of **s**. The reason is thought to be due to the electron diffraction channeling [150]. The electron diffraction channeling is described as the excitation of the coherent Bloch wave whose probability at the atom positions depends on the direction of the incident electrons, the diffraction condition and penetration depth of the specimen. The channeling effect appears notably high at the exact Bragg condition (**s**=0) and decreases as increasing the value of **s**. The channeling effect induces relatively high concentration of point defect to provide high value of λ.

The next experiment consists of in-situ observation of cascade damages in Ge produced by 20 and 30keV Xe^+ ions under the isochronal annealing from 300 to 670K in the HVEM. **Figure 7.7** shows the area density of cascade contrasts induced by irradiation with 30keV Xe^+ ions as a function of annealing temperature. The density of cascade contrasts decreases with

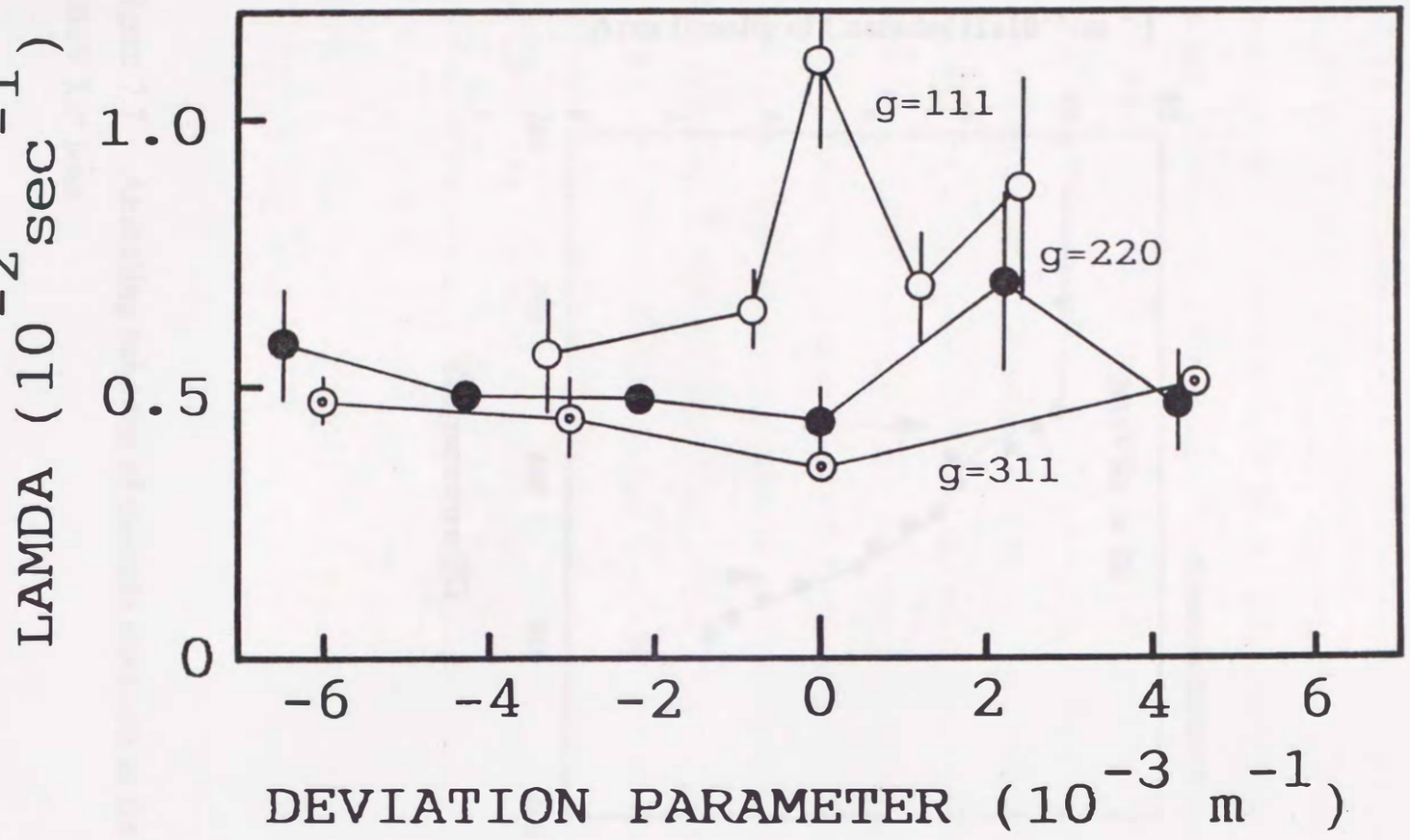

Figure 7.6 Annihilation constant of cascade contrasts, λ, as functions of reflection vector (g) and deviation parameter (s).

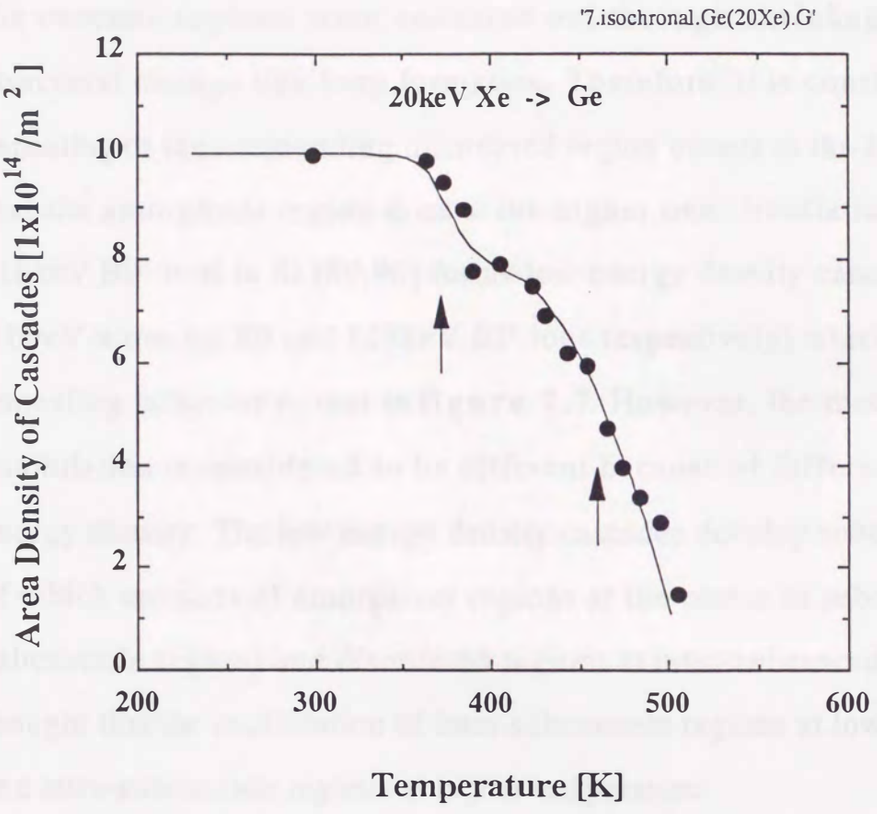

Figure 7.7 Annealing behavior of cascade contrasts in Ge irradiated with 20keV Xe^+ ions.

increasing temperature, showing two stages around 380K and 460K. 30keV Xe^+ ions generate high energy density cascades (~1eV/atom) in Ge. The cascade damages form the amorphous regions and the surrounding disordered regions as observed in **chapter 4**. In addition, in-situ observation indicates the cascade regions were annealed out through shrinkage without any structural change like loop formation. Therefore, it is considered that the annealing of the surrounding disordered region occurs at the lower stage and that the amorphous region does at the higher one. Irradiation with 80 and 118keV Bi^+ ions in Si [89,90] forms low energy density cascades (0.16 and 0.09eV/atom for 80 and 118keV Bi^+ ions respectively) which show similar annealing behavior to that in **figure 7.7**. However, the mechanism of the annihilation is considered to be different because of different value of the energy density. The low energy density cascades develop subcascades, either of which consists of amorphous regions at the center of subcascades (intra-subcascade region) and disordered regions at inter-subcascade regions. It is thought that the annihilation of inter-subcascade regions at lower temperature and intra-subcascade regions at higher temperature.

7.4. CONCLUSIONS

The stability of cascade damages has been investigated in this chapter. Cascade contrasts disappear without any other structural changes, such as loop formation, under irradiation with 0.1~1.25MeV electrons, depending on electron energy, dose rate and observation conditions. They also annealed out at temperatures from 300K to 670K during isochronal annealing. The annihilation process has been described as contributions of atomic displacements and of irradiation-induced migration of point defects. The electron energy dependence has revealed that the threshold energy of point defects being attributable to annihilation of cascade damages has been estimated as 33eV and that the effect of the atomic displacements is 6700 times higher than that of the induced-migration. However, below 700keV where electrons produce no point defects, only the induced migration is ascribed to the annihilation. The observation of shrinkage and annihilation of cascade regions and the results of the isochronal annealing indicate the annealing of the surrounding disordered regions at 380K and that of the amorphous regions at 460K.

CHAPTER 8

SUMMARY AND FUTURE PROSPECTS

8.1. SUMMARY

Studies on the structure, the accumulation process and the stability of cascade damages are indispensable for the development of irradiation-resistant nuclear materials. Stimulated by the fundamental interest as well as the practical importance, studies have been performed on non-metallic inorganic materials including semiconductors with use of the HVEM-ACC facilities. The facility is expected to be one of conclusive methods for understanding the ion-induced phenomena, because of its easy control of experimental parameters and in-situ observation. The HVEM-ACC facility at KU comprising of an ion accelerator and a VTR imaging system and the HVEM-Tandem Facility at ANL has been extensively used in this study.

The conclusions obtained in **chapters 4** to **7** are summarized as follows:

In **chapter 4**, cascade damages produced by 30keV Xe^+ ions have been characterized as functions of ionicity and mass of target atoms through transmission electron microscopy (TEM). In covalent high-Z materials, such as Si and Ge, cascade damages show up their contrasts; nor in ionic low-Z materials. Further discussion has been done on cascade contrasts in Si, Ge and Ge-Si alloys through TEM images. Cascade regions show up structure factor contrast and strain contrast, either of which respectively mentions the existence of amorphous and strained (disordered) regions. The amorphous

regions have been observed as being surrounded by disordered regions through the melted zone and the subsequent quenching.

The energy of PKAs distributes widely in a material under fission and fusion environments, introducing isolated point defects and electronic excitation as well as cascade damages. The concurrent irradiation with ions and electrons have been extensively done for understanding the concurrent effect on the accumulation process of cascade damages in **chapter 5** and that on ion-induced amorphization in **chapter 6**. The understanding of the concurrent effect also helps to acquire insights into the nature of cascade damages, such as the structure and the stability of cascade damages.

In **chapter 5**, the accumulation process of cascade has been examined under irradiation with 30keV Xe^+ ions and 250~1000keV electrons. The density of cascade contrasts increases with increasing ion dose eventually leading to saturation. The process of the cascade accumulation, which depends on ion species, incident energy and mass of target atoms, indicates that cascade contrasts appear with help from other cascade damages. The help is concluded to be due to the overlaps of cascade damages or plasticity spikes (shock wave) from analysis of the experimental results based on the kinetic equation taking into account the concurrent effect of simultaneous electron irradiation.

In **chapter 6**, the irradiation-induced amorphization in Si and the dual-beam irradiation effects on the amorphization have been done. The effect of simultaneous electron irradiation on ion-induced amorphization has been observed as the prevention and the retardation of ion-induced amorphization and as retention of crystallinity. The dual-beam irradiation with a focused electron beam and homogeneous ions forms the interface of crystalline and

amorphous phases. The position of the interface has been converted to the critical electron dose rate enough to prevent specimen from amorphization. The critical electron dose rate depends ion species, ion energy and ion dose rate, and it has been used for getting conclusive remarks that amorphous embryos are essentially subcascades and that the overlap of subcascades leads crystalline Si to amorphous. The critical electron dose rate depends also on electron energy, showing the more effectiveness of lower energy electrons for the retardation. From the results it has been concluded that the irradiation-induced amorphization under the concurrent irradiation with ions and electrons is controlled by a synergistic effect of cascades and electronic excitations.

In **chapter 7**, the further investigations have been extended both to the annihilation process under continuous irradiation with electrons and isochronal annealing. Cascade regions in Ge annihilate during electron irradiation depending on electron dose rate, electron energy and irradiation conditions. The annihilation constant increases linearly with the electron dose rate, suggesting the kinetics controlled by interstitial atoms. The electron energy dependence of the annihilation constant, however, suggests that some part of the annihilation process is controlled by the irradiation-induced migration of point defects. The amorphous regions and surrounding disordered regions thermally recover at 380K and 460K during isochronal annealing, respectively.

8.2. FUTURE PROSPECTS

Concurrent effects of dual-beam irradiation with ions and electrons in Si and Ge have been investigated in this work. It is realized that the advantage of HVEM-ACC facilities is easy control of production rate of cascades, point defects, athermal migration of point defects and electronic excitation. Therefore, HVEM-ACC facilities are one of suitable facilities to prospect radiation damages in fission and fusion nuclear materials. In this section, the author expresses future prospects of HVEM-ACC facilities as the facility giving fruitful simulation of radiation damages under fusion environments. Concurrent effect of cascades, isolated point defects and others under fusion environments is also discussed in this section.

Fission reactors, ion accelerators and HVEM have been extensively used for prediction of radiation damages induced by fusion neutrons. Especially ions and fission neutrons have been thought to give successful simulation of radiation damage of fusion neutrons. However, the difference of PKA energy spectra among fusion neutrons and others has been pointed out. Low energy PKAs are rather dominant under irradiation with ions and fission neutrons in comparison to fusion neutrons. Under the circumstance, isolated point defects are generated dominantly and their behavior becomes important. Furthermore, it is impossible to vary the PKA energy spectra in those experiments. On the contrary, one of advantages of HVEM-ACC facilities is easy control of fractional variations of high energy PKAs to low energy ones. The variation is expected to give a successful simulation of radiation damages under irradiation with fusion neutrons and/or to give insights into the

correlation among irradiation experiments with ions, fission neutrons and fusion ones.

The production rates of isolated point defects and cascade damages are important factors for simulating fusion environments. The number of isolated point defects induced by low energy PKAs is calculated with the NRT model [151]. In case of cascade damages, their number induced by high energy PKAs is evaluated simply with $0.4T/E_d^c$, where T and E_d^c are, respectively, PKA energy and the threshold energy of subcascade formation (15keV for Si). The differential cross sections were calculated for various elements by Shimomura et al. [152]. The number of point defects and cascade damages and their differential cross sections give the production rate of point defects and that of cascade damages by a fusion neutron, and they are estimated as $2.2x10^{-27}$ and $3.6x10^{-27}$, respectively. The production rate of subcascades is larger than that of isolated point defects. As shown in **table 1.2**, the expected dose rate of neutrons at the first wall is 10^{19} n/m^{2}s. Therefore, the production rates of isolated point defects and of cascade damages are estimated as $\mathbf{2.2x10^{-6}}$ and $\mathbf{3.6x10^{-6}}$/s for the irradiation with 14MeV neutrons, respectively.

In case of HVEM-ACC facilities, the displacement cross section of 1MeV and 200keV electrons in Si are, respectively, about 53 and 11 barns. A representative electron dose rate is 10^{23} e/m^{2}s, and gives $\mathbf{5.3x10^{-4}}$ and $\mathbf{1.1x10^{-4}}$/s for the production rate of the isolated point defects under irradiation with 1MeV and 200keV electrons, respectively. For 30keV Xe^+ ions, all of ions generate cascade damages within a volume consisting of the longitudinal range (~20nm) and the radial range (~6nm). The number of atoms within the spheroid is estimated as $7.7x10^4$ atoms. Therefore, the cross

section of 30keV Xe^+ ions is calculated as $\pi \cdot 6^2/7.7 \times 10^4$ nm^2 = 2.5×10^7 barns. Multiplication of the cross section with a representative ion dose rate of 10^{16} ions/m^2s gives **2.5×10^{-5}**/s of the production rate of cascades. The same range of ratios of the production rates of cascade damages and isolated point defects under fusion environments is available in HVEM-ACC facilities with comparing the cross sections of 14MeV neutrons and the experimental condition in this work. It should be noted, however, that the production rate of isolated point defects and cascade damages in HVEM-ACC facilities are, respectively, one and two orders higher than those in first wall environments. The possible minimum dose rates of ions and electrons are, respectively, ~10^{14} ions/m^2s and ~10^{22} e/m^2s, both of which are still higher than the first wall condition. To develop more suitable method of the simulation, one should realize much lower ion and electron dose rates.

The accumulation process of cascade damages in Si and Ge has been investigated under irradiation with ions and electrons, and the process is described as the retardation of the accumulation of cascade damages. The analogous process will be observed under fusion environments. Eq.(5.11) predicts the accumulation and the annihilation of cascade damages under fusion environments, though the production rate of cascade damages in fusion reactors is about one order of magnitude lower than in HVEM-ACC facility. According to eq.(5.11), the density of cascade damages increases with irradiation time, and it reaches saturation level after considerably long irradiation time (~1000s) under fusion environments. The dose rate dependence on irradiation-induced amorphization in Si has been investigated. As revealed in **figure 6.7**, the damage rate for preventing amorphization increases with increasing that for amorphization and obeying $\phi_e^c \propto (\phi_i)^x$. The

power x of the increasing curve depends on ion species especially in lower ion dose rate regions, and it is described by the mean distance of independent subcascades resulting in amorphization. The lighter ions like Ar^+ shows relatively high value of the power, or it depends strongly on dose rates. In case of irradiation with fusion neutrons, since their mean free path is of the order of cm and the target consists of low-Z elements, the dose rate dependence becomes significant. In other words, it is expected that the amorphization induced by irradiation would be prevented or retarded by isolated point defects. Throughout this chapter, neither the effect of athermal migration of point defects nor that of electronic excitation is taken into account. Further insights into their effects will be required.

The advantages of the HVEM-ACC interface are easy control of the experimental conditions, such as ion species, ion energy, electron energy, dose rate of ions and electrons, their dose, irradiation temperature and observation condition. They bring us the precise insights into the concurrent effects and the radiation damage under fusion and fission environments. The author hopes to develop the radiation-resistant nuclear materials through fundamental studies with use of the HVEM-ACC interface in the future.

ACKNOWLEDGEMENTS

First and foremost, the author wishes to express his sincere appreciation to his advisor, Professor Chiken Kinoshita. His encouragement and guidance have made the author's graduate study a very rewarding experience.

He would also like to thank Professors Masayasu Sugisaki, Yasunori Hayashi and Naoaki Yoshida at Kyushu University and Drs. Paul R. Okamoto and Lynn E. Rehn at Argonne National Laboratory for their valuable advice, suggestions and guidance.

He also acknowledges Associate Professors Kazutoshi Shinohara at Kumamoto Institute of Technology, Kiyomichi Nakai at Ehime University and Sho Mastumura at Kyushu University for valuable discussion.

Appreciation is also extended to Messrs. Masanori Kustuwada, Eishi Tanaka, Takeshi Manabe, Yasutaka Denda and Takeshi Sonoda at Kyushu University and to Messrs. Bernard J. Kestel, Edward A. Ryan, Stanley T. Osckers and Loren L. Funk at Argonne National Laboratory for their experimental and technical assistance.

He is grateful to his parents and fiancée Nastuko for their support and encouragement of his school days.

REFERENCES

[1] Clinard, F.W.Jr. and Hobbs, L.W.: 'Physics of Radiation Effect in Crystals' ed. by Johnson, R.A. and Orlov, A.N. (Elsevier Science B.V., 1986) p.387.

[2] Hopkins, G.R. and Price, R.J.: Nucl. Eng. Design/Fusion 2, 111 (1985).

[3] Kiritani, M.: J. Nucl. Mater. 179-181, 81 (1991).

[4] Jesser, W.A.: IEEE Trans. Nucl. Sci. NS26, 1252 (1979).

[5] Haga, K., King, W.E., Merkle, K.L. and Meshii, M.: Nucl. Instrum. Meth. Phys. Res. B16, 134 (1986).

[6] Taylor, A., Allen, C.W. and Ryan, E.A.: Nucl. Instrum. Meth. Phys. Res. B24-25, 598 (1987).

[7] Allen, C.W., Funk, L.L., Ryan, E.A. and Taylor, A.: Nucl. Instrum. Meth. Phys. Res. B40-41, 553 (1988).

[8] Vetrano, J.S., Bench, M.W., Robertoson, I.M. and Kirk, M.A.: Metall. Trans. A20, 2673 (1989).

[9] Robertson, I.M., Vetrano, J.S., Kirk, M.A. and Jenkins, M.L.: Philos. Mag. A63, 299 (1991).

[10] Abe, H., Kinoshita, C. and Nakai, K: J. Nucl. Mater. 179-181, 917 (1991).

[11] Fukumoto K., Kinoshita, C., Abe, H., Shinohara, K. and Kutsuwada, M.: J. Nucl. Mater. 179-181, 935 (1991).

[12] Kinoshita, C.: J. Nucl. Mater. 179-181, 53 (1991).

[13] Kinoshita, C.: Ultramicroscopy 39, 205 (1991).

[14] Takeyama, T., Ohnuki, S. and Takahashi, H.: J. Nucl. Mater. 133-134, 571 (1985).

[15] Ohnuki, S., Takahashi, H., Takeyama, T. and Nagasaki, R.: J. Nucl. Mater. 141-143, 758 (1986).

[16] Suzuki, K., Shigenaka, N., Hashimoto, T. and Nishimura, E.: Nucl. Instrum. Meth. Phys. Res. B24/25, 591 (1987).

[17] Shigenaka, N., Hashimoto, T. and Fuse, M.: Jpn. J. Appl.Phys. 1, Regul. Rap. Short Notes 28, 150 (1989).

[18] Shigenaka, N., Hashimoto, T. and Fuse, M.: The 2nd Int. Symp. Advanced Nucl. Ener. Res. (1990) p.408.

[19] Hojou, K., Furuno, S., Otsu, H., Izui, K. and Tsukamoto, T.: J. Nucl. Mater. 155-157, 298 (1988).

[20] Furuno, S., Hojou, K., Izui, K., Kamigaki, N. and Kino, T.: J. Nucl. Mater. 155-157, 1149 (1988).

[21] Hojou, K. and Izui, K.: J. Nucl. Mater. 160, 147 (1988).

[22] Hojou, K., Jitsukawa, S., Suzuki, M., Hamada, S. and Hishinuma, A.: J. Nucl. Mater. 179-181, 496 (1991).
[23] Hojou, K., Furuno, S. and Izui, K.: J. Electron Microscopy 40, 157 (1991).
[24] Muroga, T., Kitajima, N. and Ishino, S.: J. Nucl. Mater. 133&134, 378 (1985).
[25] Ishino, S., Sekimura, N., Hirooka, K. and Muroga, T.: J. Nucl. Mater. 141&143, 776 (1986).
[26] Ishino, S., Sekimura, N. and Muroga, T.: Mater. Sci. Forum 15-18, 1105 (1987).
[27] Ishino, S., Sekimura, N., Sakaida, H. and Kanzaki, Y.: Mater. Sci. Forum 97-99, 165 (1992).
[28] Seidman, D.N., Averback, R.S., Okamoto, P.R. and Baily, A.C.: Phys. Rev. Lett. 58, 900 (1987).
[29] Kimoto, T., Allen, C.W. and Rehn, L.E.: Spring Meeting of Japan Institute of Metals (1991).
[30] Ohnuki, S., Iwama, T. and Takahashi, H.: Spring Meeting of Japan Institute of Metals (1992).
[31] Abe, H., Kinoshita, C. and Okamoto, P.R.: Fall Meeting of the Atomic Energy Society of Japan (1992).
[32] Koike, J.: Ph.D. Thesis, Northwestern University (1989).
[33] Gusev, V.M., Guseva, M.I. and Starinin, C.V.: Rad. Eff. 15, 251 (1972).
[34] Washburn, J., Murty, C.S., Sanada, D., Byrne, P., Gronsky, R., Cheung, N. and Kilaas, R.: Nucl. Instrum. Meth. 209/210, 345 (1983).
[35] Wang, K., Spitzer, W.G., Hubler, G.K. and Sanda, D.K.: J. Appl. Phys. 58, 4553 (1985).
[36] Hecking, N., Heidemann, K.F. and Te Kaat, E.: Nucl. Instrum. Meth. Phys. Res. B15, 760 (1986).
[37] Elliman, R.G., Williams, J.S., Brown, W.L., Leiberich, A., Maher, D.M. and Knoell, R.V.: Nucl. Instrum. Meth. Phys. Res. B19/20, 435 (1987).
[38] Linder, J.K.N., Domres, R. and Te Kaat, E.H.: Nucl. Instrum. Meth. Phys. Res. B39, 306 (1989).
[39] Zeng, P., Ruault, M.-O., Denanot, M.F., Descouts, B. and Krauz, P.: J. Appl. Phys. 69, 197 (1991).
[40] Jencic, I., Bench, M.W., Robertson, I.M. and Kirk, M.A.: J. Appl. Phys. 69, 1287 (1991).
[41] Lindhard, J., Nielsen, V., Scharff, M. and Thomsen, P.V.: kgl. Danske Vidensk. Selsk. mat.-fys. Medd. 33, no.10 (1963).
[42] Lindhard, J., Scharff, J. and Schiøtt, H.E.: kgl. Danske Vidensk. Selsk. mat.-fys. Medd. 33, no.14 (1963).

[43] Lindhard, J. and Winther, A.: kgl. Danske Vidensk. Selsk. mat.-fys. Medd. 34, no.4 (1964).
[44] Lindhard, J., Nielsen, V. and Scharff, M.: kgl. Danske Vidensk. Selsk. mat.-fys. Medd. 36, no.10 (1968).
[45] Lindhard, J.: Proc. Roy. Soc. A311, 11 (1969).
[46] Winterbon, E.B.: kgl. Danske Vidensk. Selsk. mat.-fys. Medd. 37, no.14 (1970).
[47] Mott, N.F.: Proc. Roy. Soc. A124, 426 (1929) and A135, 429 (1932).
[48] McKinley, W.A. and Feshbach, H.: Phys. Rev. 74, 1759 (1948).
[49] Oen, O.S.: ORNL-4897 (1973).
[50] Kiritani, M.: J. Phys. Soc. Jpn. 40, 1035 (1976).
[51] Itoh, N.: '*Housya-sen Bussei* I', *Morikita Shuppan*, Tokyo (1981) [in Japanese].
[52] Kinchin, G.H. and Pease, R.S.: Repts. Progr. Phys. 18, 1 (1955).
[53] Bourret, A.: Int. Conf. on Vac. and Intersti. in Metals, Jülich (1968). p.377
[54] Shimomura, Y.: Philos. Mag. 19. 773 (1969).
[55] Makin, J.: Philos. Mag. 20, 1133 (1969).
[56] Kiritani, M.: Bull. Jpn. Institute of Metals 116, 13 (1974) in Japanese.
[57] Hirata, M. and Kiritani, M.: Physica 116B, 623 (1983).
[58] Kinoshita, C., Hayashi, K. and Kitajima, S.: Nucl. Instrum. Meth. Phys. Res. B1, 209 (1984).
[59] Kinoshita, C. and Nakai, K.: Jpn. J. Appl. Phys. Series 2, Lattice Defects in Ceramics (1989) p.105.
[60] Yougman, R.A., Hobbs, L.W. and Mitchell, T.E.: J. de Physique. C6, 227 (1980).
[61] Edington, J.W.: 'Practical Electron Microscopy in Materials Science' (Van Nostrand Reinhold Company, New York, 1796).
[62] Bell, W.L.: J. Appl. Phys. 47, 1676 (1976).
[63] Sulisbury, I.G.: J. Microscopy 118, 75 (1980).
[64] Stathopoulos, A.Y. and Pells, G.P.: Philos. Mag. A47, 381 (1983).
[65] Howitt, D.G. and Mitchell, T.E.: Philos. Mag. A44, 229 (1980).
[66] Nakai, K., Fukumoto, K. and Kinoshita, C.: J. Nucl. Mater. 191-194, 630 (1992).
[67] Ziegler, J.F., Biersack, J.P. and Littmark, U.: 'The Stopping and Range of Ions in Solids' (Pergamon Press Inc., Oxford, 1985).
[68] Ziegler, J.F.: 'Helium Stopping Powers and Ranges in All Elemental Matter' (Pergamon Press Inc., Oxford, 1977).
[69] Brice, D.K.: 'Ion Implantation Range and Energy Deposition Distributions vol.1' (Plenum, New York, 1975).
[70] Winterbon, K.B.: 'Ion Implantation Range and Energy Deposition Distributions vol.2' (Plenum, New York, 1975).
[71] Sigmund, P.: Appl. Phys. Letts. 25, 169 (1974).

[72] Averback, R.S., Diaz de la Rubia, T. and Benedek, R.: Nucl. Instrum. Meth. Phys. Res. B33, 693 (1988).
[73] Averback, R.S. and Seidman, D.N.: Materials Science Forum 15-18, 963 (1987).
[74] Guinan, M.W. and Kinney, J.H.: J. Nucl. Mater. 103&104, 1319 (1981).
[75] Andersen, H.H. and Bay, H.L.: J. Appl. Phys. 45, 953 (1974).
[76] Moore, J.A., Carter, G. and Tinsley, A.H.: Rad. Eff. 25, 49 (1975).
[77] Thompson, D.A.: Rad. Eff. 56, 105 (1981).
[78] Brinkman, J.A.: J. Phys. 24, 246 (1956).
[79] Brinkman, J.A.: J. Appl. Phys. 25, 961 (1954).
[80] Seitz, J. and Koehler, J.S.: Solid State Phys. 2, 30 (1965).
[81] Ishino, S.: '*Shousha-Sonshou*' (Tokyo University Press, Tokyo, 1979) [in Japanese].
[82] Stoneham, A.M.: Philos. Mag. 36, 983 (1977).
[83] Thompson, D.A. and Walker, R.S., Davies, J.A.: Rad. Eff., 32, 135 (1977).
[84] Thompson, D.A. and Walker, R.S.: Rad. Eff., 36, 91 (1978).
[85] Andersen, H.H. and Bay, H.L.: Rad. Eff., 19, 139 (1973).
[86] Pronko, P.P., Mitchell, J.B., Shewchen, J. and Davies, J.A.: Rad. Eff., 20, 257 (1973).
[87] Walker, R.S. and Thompson, D.A.: Nucl. Instrum. Meth., 135, 489 (1976).
[88] Thompson, D.A.: Nucl. Inst. Meth., 170, 419 (1980).
[89] Howe, L.M. and Rainville, M.H.: Nucl. Instrum. Meth., 182-183, 143 (1981).
[90] Howe, L.M. and Rainville, M.H.: Nucl. Instrum. Meth. Phys. Res., B19-20, 61 (1987).
[91] Walker, R.S., Thompson, D.A.: Rad. Eff., 37, 113 (1978).
[92] Ruault, M.O., Chaumont, J. and Bernas, H.: Nucl. Instrum. Meth., 170, 419 (1980).
[93] Ruault, M.O., Chaumont, J., Penisson, J.M. and Bourret, A.: Philos. Mag. A50, 667 (1984).
[94] Guinan, M.W.: J. Nucl. Mater., 53, 171 (1974).
[95] Kiritani, M., Yoshiie, T., Kojima, S. and Satoh, Y.: Rad. Eff., 113, 75 (1990).
[96] Bohr, N.: Philos. Mag., 25, 10 (1913).
[97] Firsov, O.B.: Soviet Phys. JETP 36, 1076 (1959).
[98] Iwase, A., Sasaki, S., Iwata, T. and Nihira, T.: Phys. Rev. Lett., 58, 2450 (1987).
[99] Iwata, T. and Iwase, A.: JAERI-memo 63-281.
[100] Iwase, A., Iwata, T., Sasaki, S. and Nihira, T.: JAERI-memo 63-336.
[101] Iwase, A.: JAERI-M 89-071(1989) [in Japanese].
[102] Averback, R.S. and Merkle, K.L.: Phys. Rev., B16, 3860 (1977).
[103] Averback, R.S. and Merkle, K.L.: Phys. Rev., B18, 4156 (1978).
[104] Hersh, H.N.: Phys. Rev., 148, 928 (1966).
[105] Fleisher, R.L.: Progress in Materials Science, 1, 97 (1981).

[106] Bowden, F.P., Chadderton, F.R.S. and L.T.: Proc. Roy. Soc., A269, 143 (1962).
[107] Hansen, P., Heitmann, M. and Smit, P.H.: Phys. Rev., B26, 3539 (1982).
[108] Fuchs, G., Studer, F., Balavzat, E., Grouly, D., Jousset, J.C. and Raveau, B.: Nucl. Ins. Meth. Phys. Res., B12, 471 (1985).
[109] Toulemonde, M., Fuchs, G., Nguyen, N., Studer, F. and Groult, D.: Phys. Rev., B35, 6560 (1987).
[110] Toulemonde, M., Studer, F.: Phil. Mag., 58, 799 (1988).
[111] Ronch, C.:J. Appl. Phys., 44, 3575 (1973).
[112] Yada, K., Tanji, T. and Sunagawa, I.: Phys. Chem. Minerals, 7, 47 (1981).
[113] Yada, K., Tanji, T. and Sunagawa, I.: Phys. Chem. Minerals, 14, 197 (1987).
[114] Lyles, R.Jr., Taylor, A., Merkle, K.L., Okamoto, P.R. and Pronko, P.: 9th Int. Conf. Elec. Microsc., Tronto (1978) p76.
[115] Wilson, I.H.: J Appl. Phys., 53, 1698 (1982).
[116] Hirata, M. and Kiritani, M.: Physica ,116B, 616 (1983).
[117] Petzow, G.: Metallographisches Ätzen, P73, (Materialkundlich-Technische Reihe 1976).
[118] Kestel, B.J.: ANL-80-120, 1986.
[119] Hayashi, K.: ME Thesis, Kyushu University (1984).
[120] Satoh, Y.: ME Thesis, Kyushu University (1990).
[121] Zebg, P., Rault, M.O., Kaitasov, O., Crestou, J., Descouts, B., Krautz, P. and Duhamel, N.: J. Phys. D23, 877 (1990).
[122] Zebg, P., Rault, M.O., Denanot, M.F., Descouts, B. and Krautz, P.: J. Appl. Phys. 69, 197 (1991).
[123] Jencic, I., Bench, M.W., Robertson, I.M. and Kirk, M.A.: J. Appl. Phys. 69, 1287 (1991).
[124] Phillips, J.C.: Rev. Modern Phys., 42, 317 (1970).
[125] Kinoshita, C.: Proceedings of ICFRM-5 (1991) to be published in J. Nucl. Mater.
[126] Rault, M.O., Chaumont, J. and Bernas, H.: Nucl. Instrum. Meth., 209/210, 351 (1983).
[127] Thompson, D.A., Glanski, A., Haugen, H.K., Howe, L.M. and Davis, J.A.: Rad. Eff. 69, 191 (1983).
[128] Thompson, D.A., Glanski, A., Haugen, H.K., Howe, L.M. and Davis, J.A.: Rad. Eff. 50, 125 (1980).
[129] Howe, L.M., Rainville, M.H., Haugen, H.K. and Thompson, D.A.: Nucl. Instrum. Meth., 170, 419 (1980).
[130] Gibbons, J.F.: Proc. IEEE 60, 1062 (1972).
[131] Nastasi, M. and Mayer, J.W.: Mater. Sci. Rep. 6, 1 (1991).
[132] Idemistu, K. and Denda, Y.: private communication.

[133] Ferreira Lima, C.A. and Howie, A.: Philos. Mag. 34, 1057 (1976).
[134] Hirata, M. and Kiritani, M.: Physica 116B, 616 (1983).
[135] Salisbury, I.G.: J. Microsc. 118, 75 (1980).
[136] Hua, G.C., Oshima, R. and Fujita, F.R.: J. Mater. Sci. 25, 328 (1990).
[137] Baranova, E.C., Gusev, V.M., Martynenko, Yu.V., Starinin, C.V. and Haibullin, I.B.: Rad. Eff. 18, 21 (1973).
[138] Morehead, F.F.Jr. and Crowder, B.L.: Proc. 1st. Int. Conf. on Ion Implantation, Ed. by Chadderton, L. and Eisen, F., Gordon and Breach, New York (1971) pp.25.
[139] Dennis, J.R. and Hale, E.B.: J. Appl. Phys. 49, 1119 (1978).
[140] Matthews, M.D. and Ashby, S.J.: Philos. Mag. 27, 1313 (1973).
[141] Föll, H.: 'Lattice Defects in Semiconductors' ed. by Huntley, F.A., IOP Conference Proceedings No.23 (Inst. Phys., Bristol and London, 1975) pp.233.
[142] King, W.E.: Ph.D. Thesis at Northwestern University (1980).
[143] Loferski, J.J. and Rappaport, P.: J. Appl. Phys. 30, 1296 (1959).
[144] Heinisch, H.L. and Singh, B.N.: submitted to Philos. Mag. (1992).
[145] Robinson, M.T. and Torrens, I.M.: Phys. Rev. B9, 5008 (1974).
[146] Bourgoin, J.C. and Corbett, J.W.: Phys. Lett. A38, 135 (1972).
[147] Bethe, H.A. and Ashkin, J.: Experimental Physics, ed. Segre, E. (Wiley, New York, 1953) vol.1, pp.166.
[148] Mayer, J.W., Eriksson, L., Picraux, S.T. and Davis, J.A.: Can. J. Phys. 46, 663 (1968).
[149] Ruault, M.O., Haumont, J. and Bernas, H.: Nucl. Inst. Methods 209/210, 351 (1983).
[150] Yoshida, N. and Urban, K.: Proc. Fifth Int. Cof. on High Voltage Electron Microscopy (Kyoto, 1977) pp.485.
[151] Robinson, M.T. and Torrens, I.M.: Phys. Rev. B9, 5008 (1974).
[152] Shimomura, Y., Nishiguchi, R., Nagata, E., Hahn, P.A., Guinan, M.W. and Kiritani, M.: private communication.

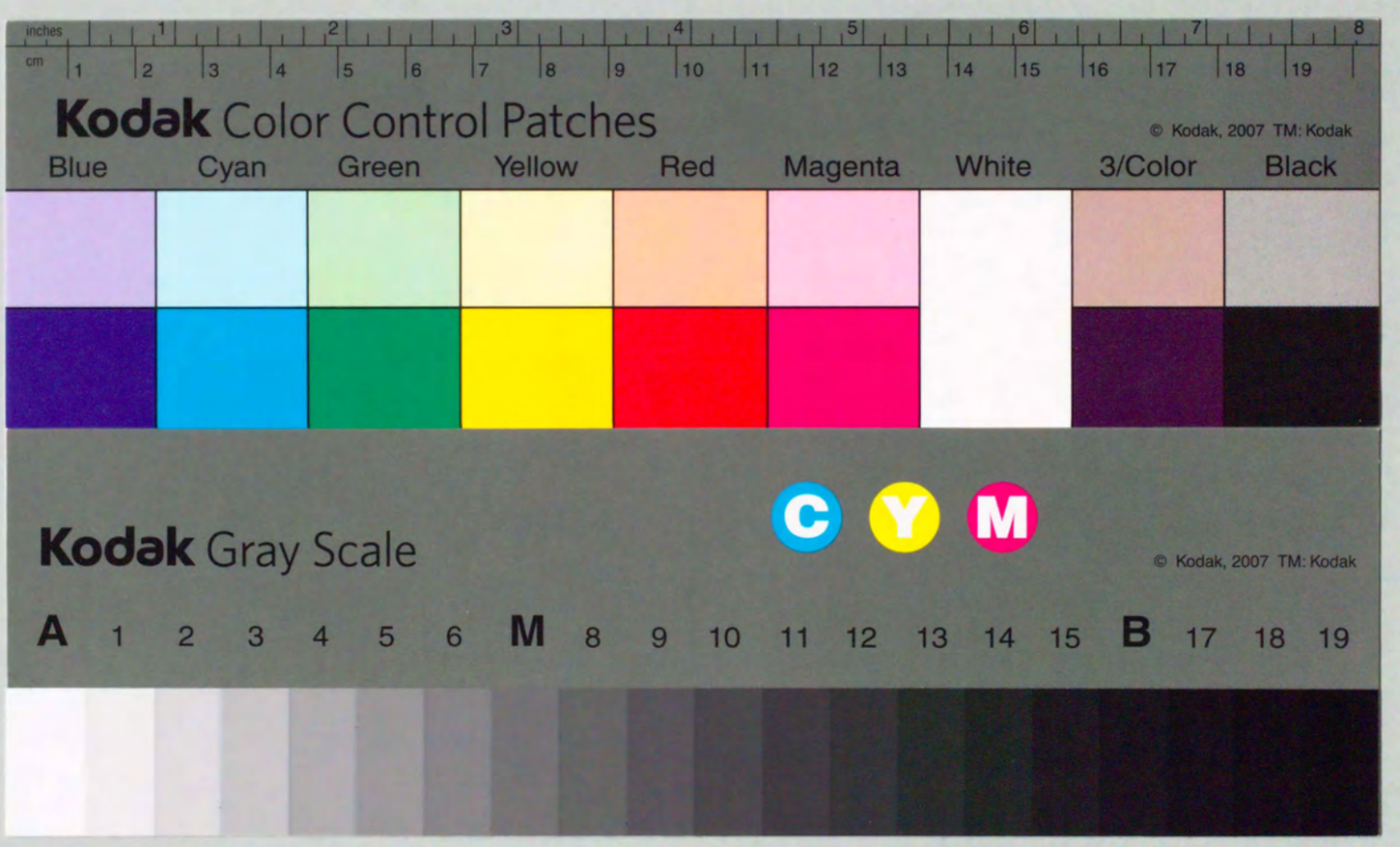
inches
cm
Kodak Color Control Patches
© Kodak, 2007 TM: Kodak
Blue
Cyan
Green
Yellow
Red
Magenta
White
3/Color
Black
Kodak Gray Scale
C
Y
M
© Kodak, 2007 TM: Kodak
A 1 2 3 4 5 6 M 8 9 10 11 12 13 14 15 B 17 18 19